

This is the author manuscript accepted for publication and has undergone full peer review but has not been through the copyediting, typesetting, pagination and proofreading process, which may lead to differences between this version and the [Version of Record](#). Please cite this article as doi: [10.1029/2018JA025543](https://doi.org/10.1029/2018JA025543)

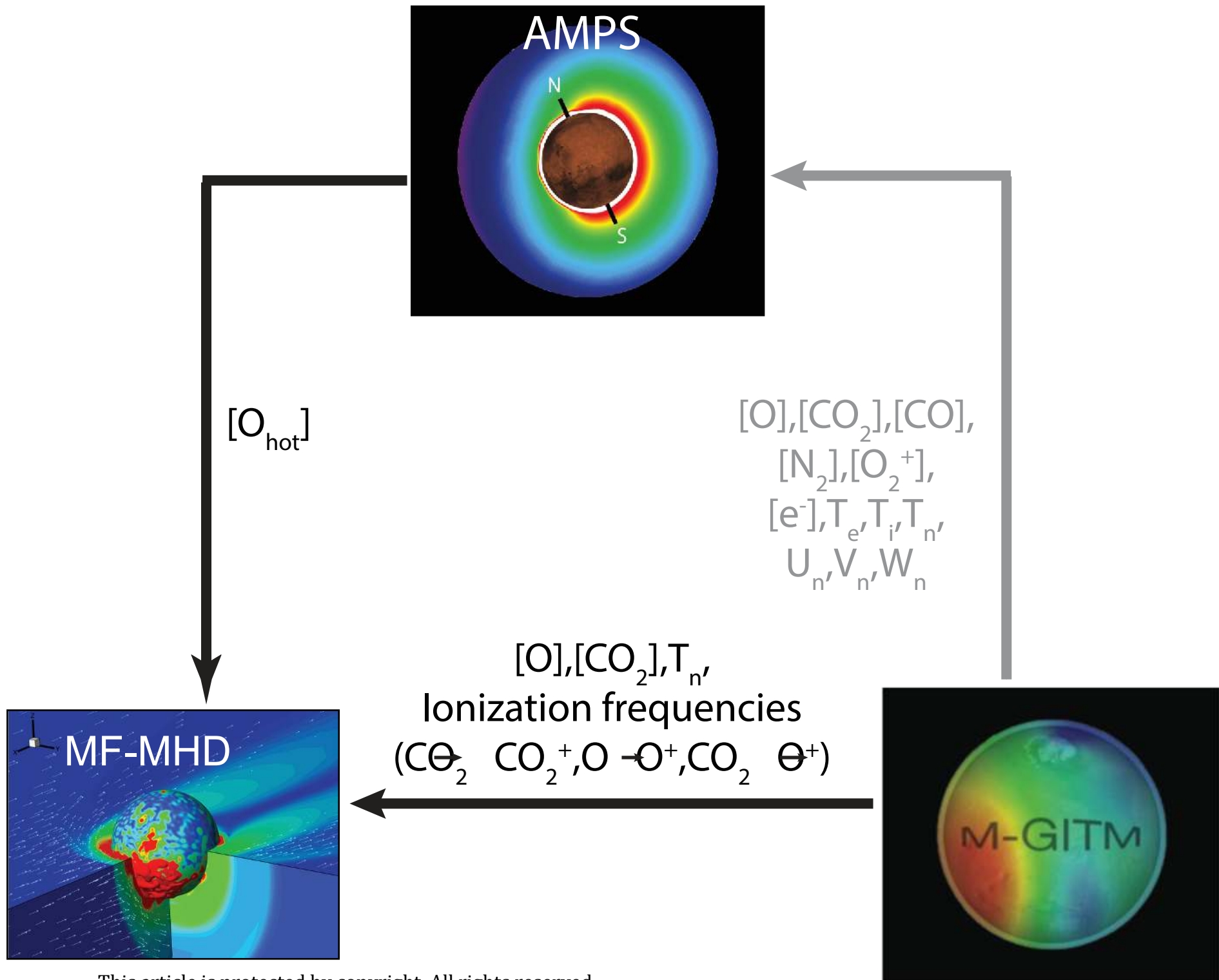
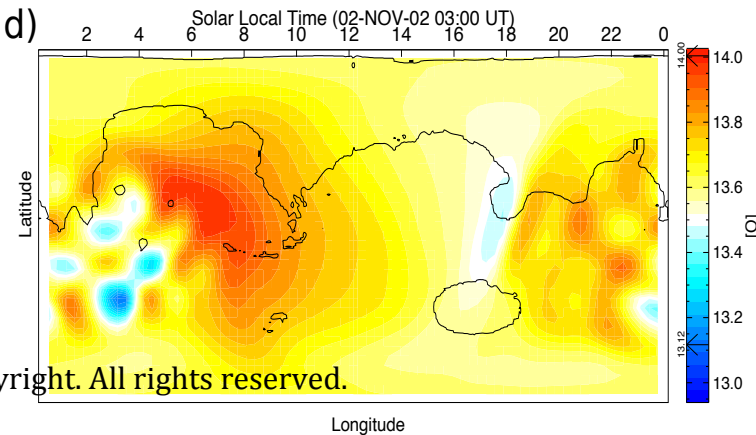
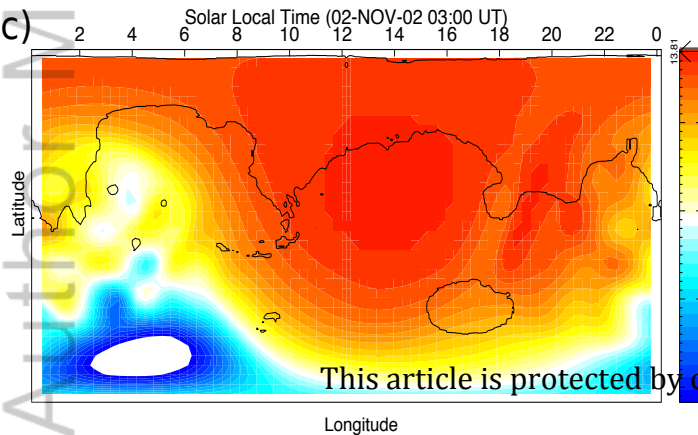
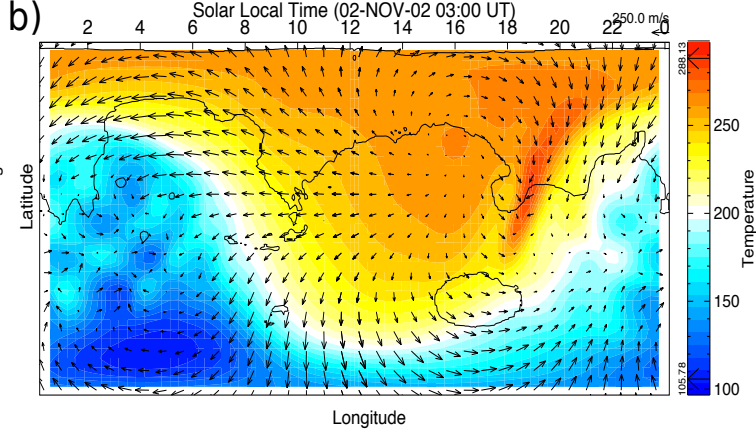
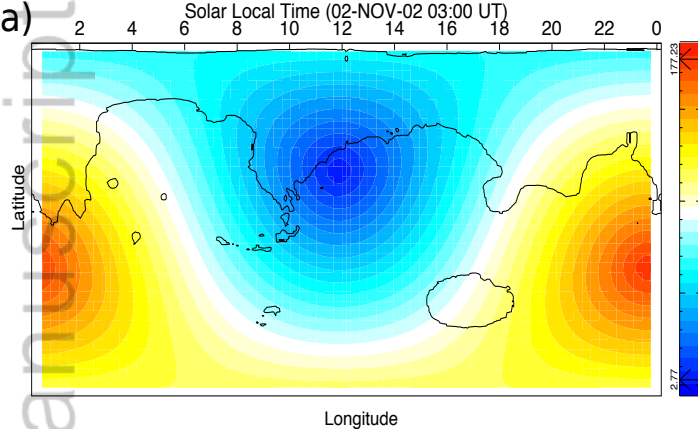


Figure 2.

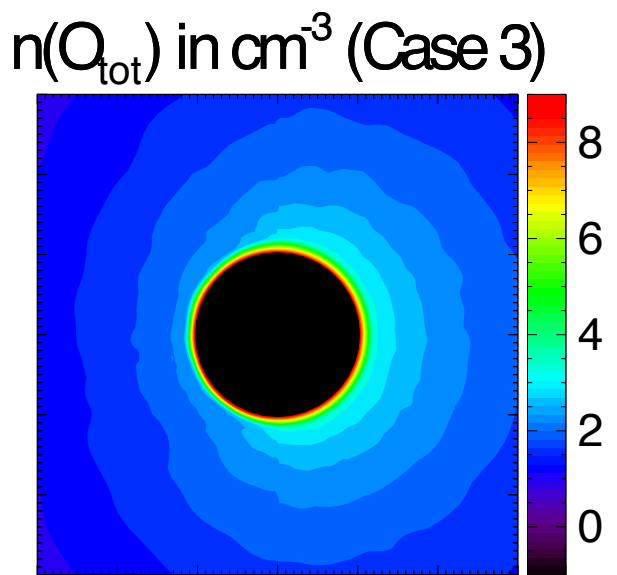
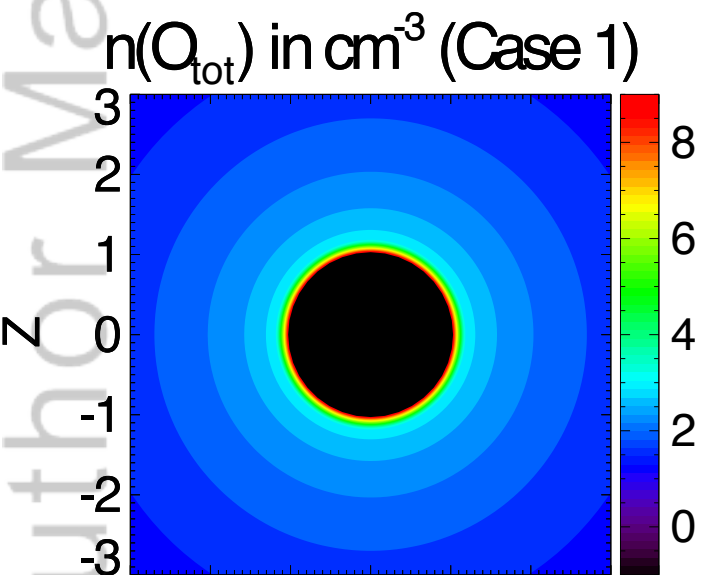
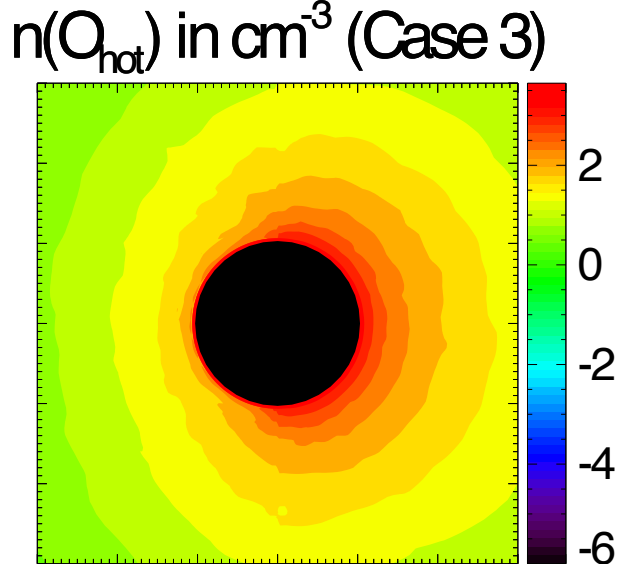
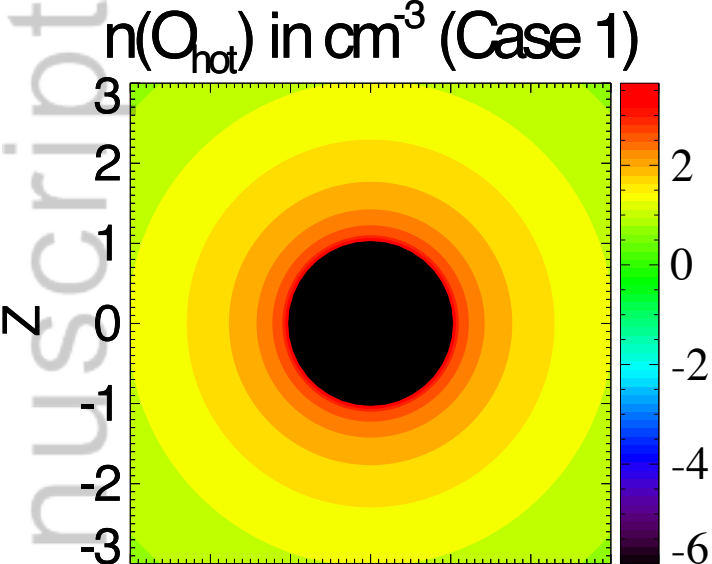
Author Manuscript



This article is protected by copyright. All rights reserved.

Figure 3.

Author Manuscript



-3 -2 -1 0 1 2 3 -3 -2 -1 0 1 2 3

This article is protected by copyright. All rights reserved.

X

X

Figure 4.

Author Manuscript

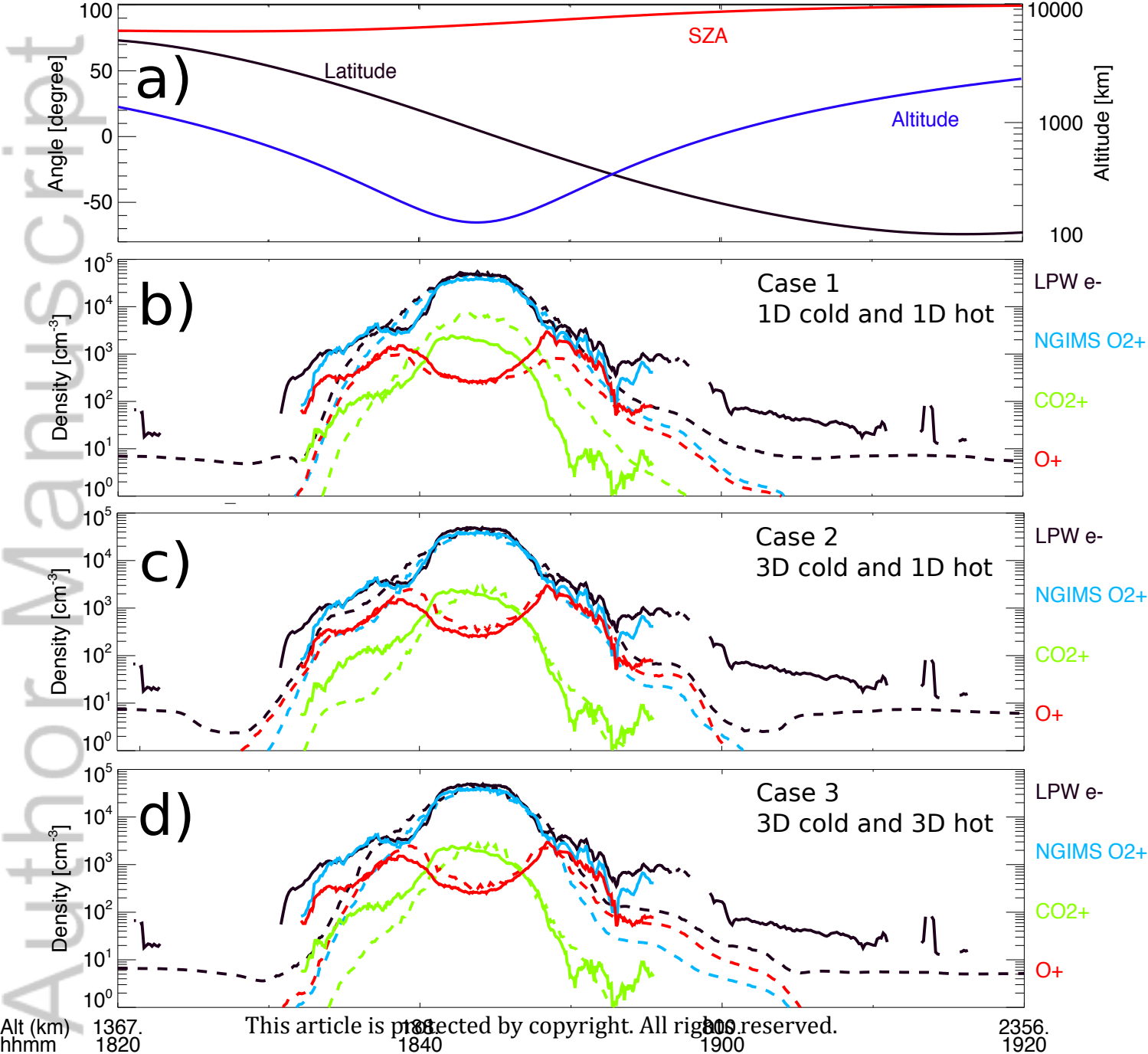




Figure 5.

Author Manuscript

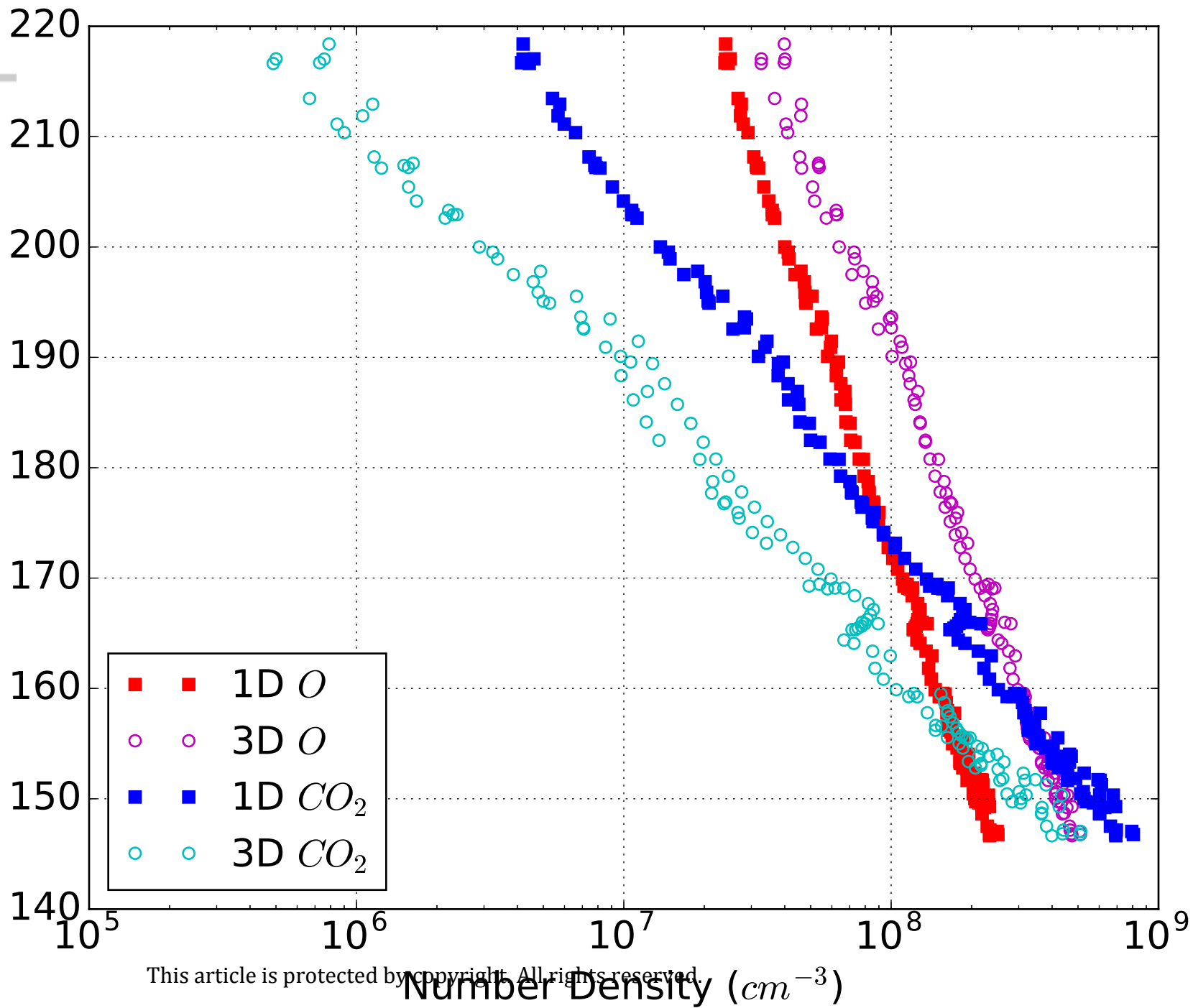


Figure 6.

Author Manuscript

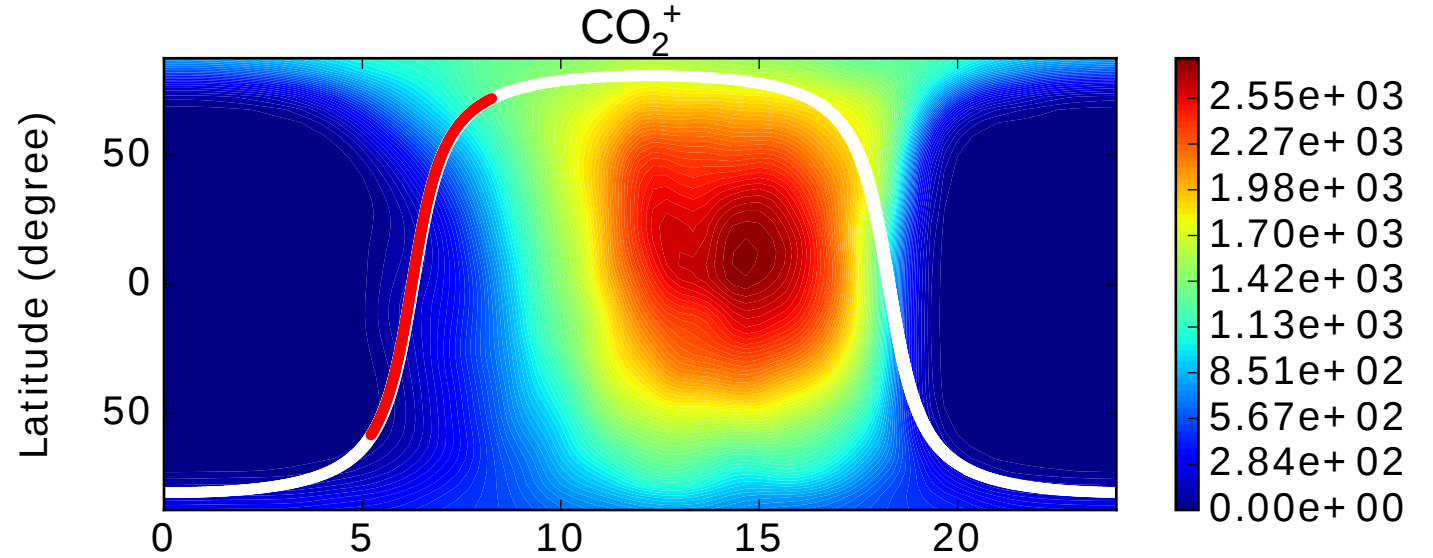
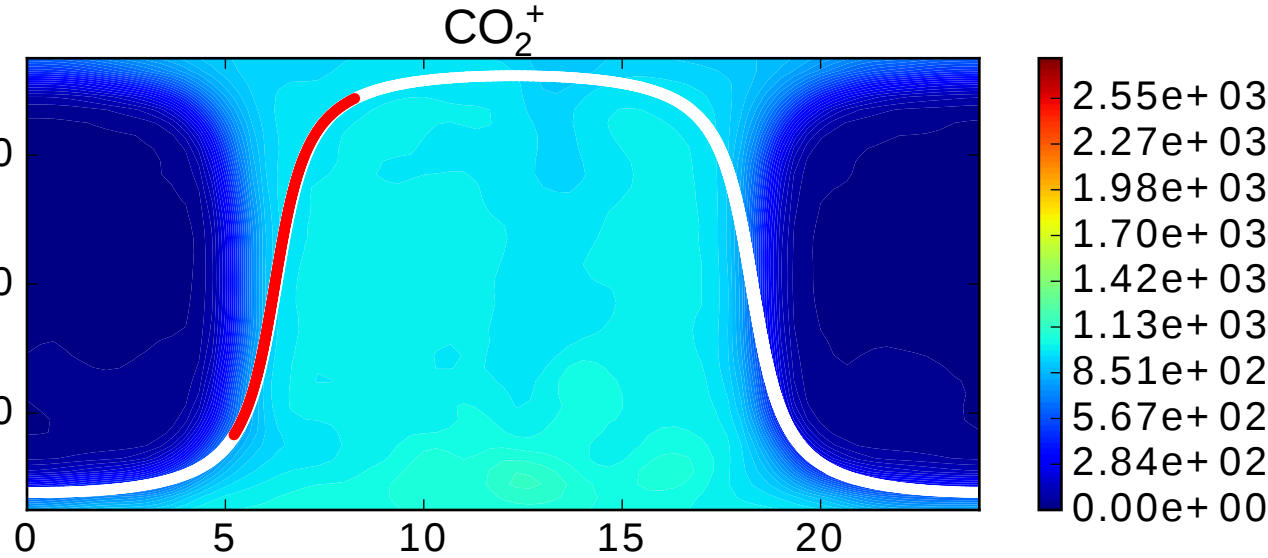
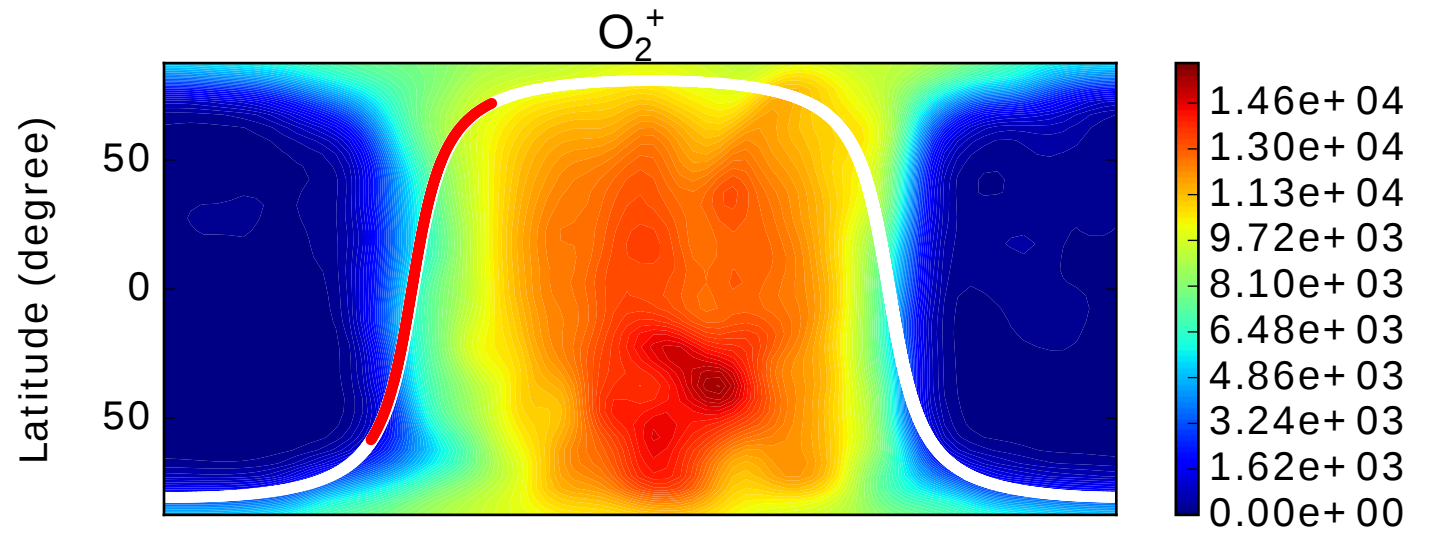
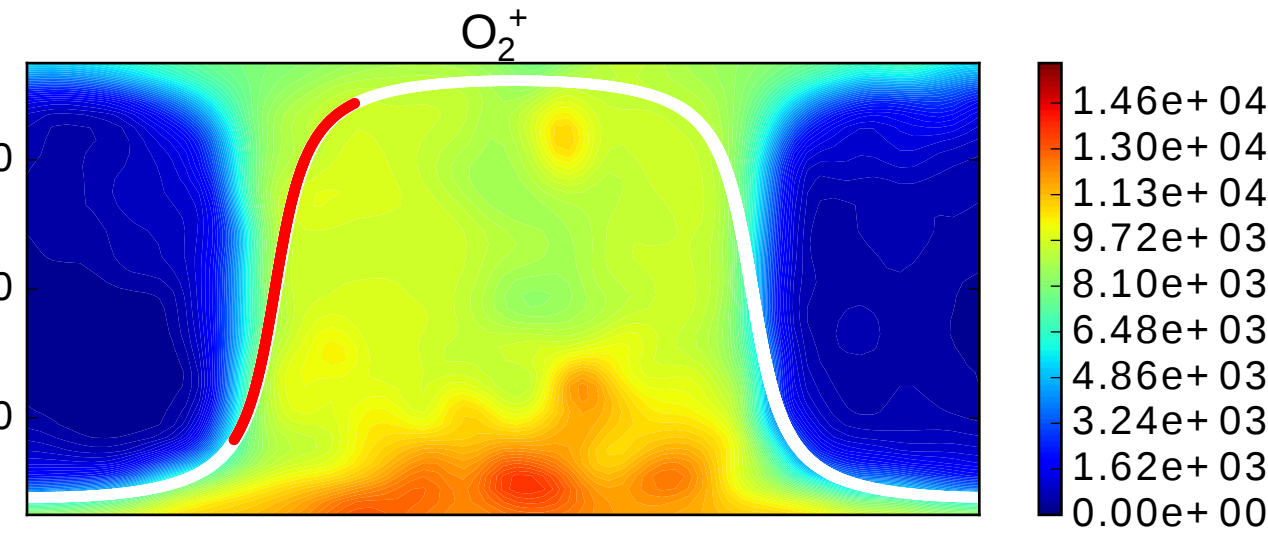
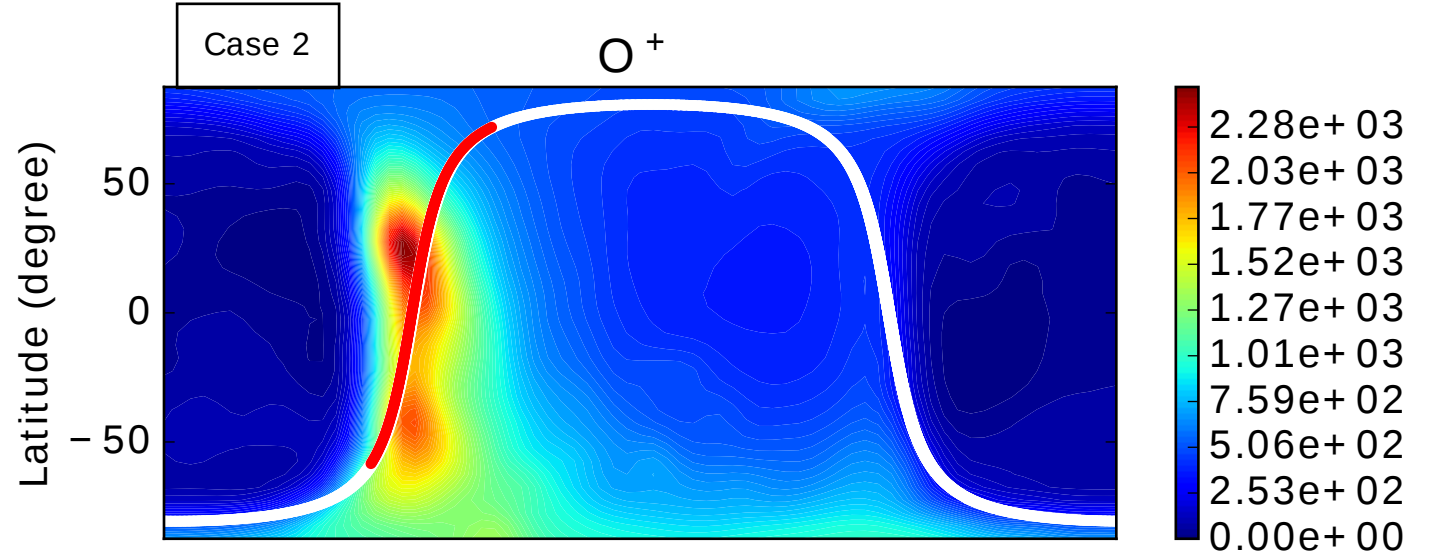
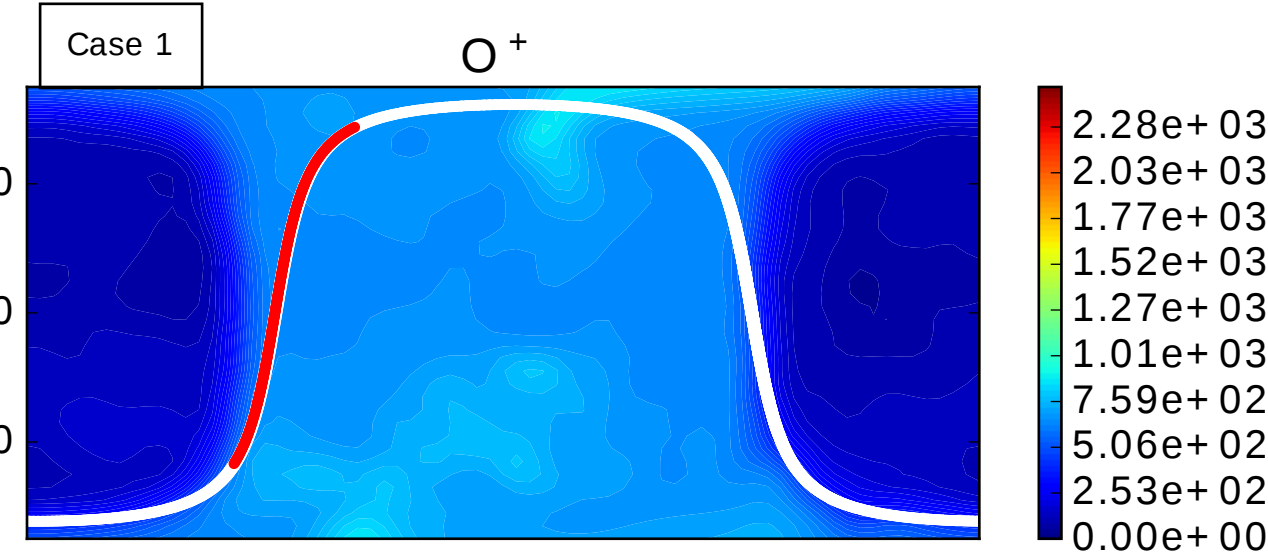


Figure 7.

Author Manuscript

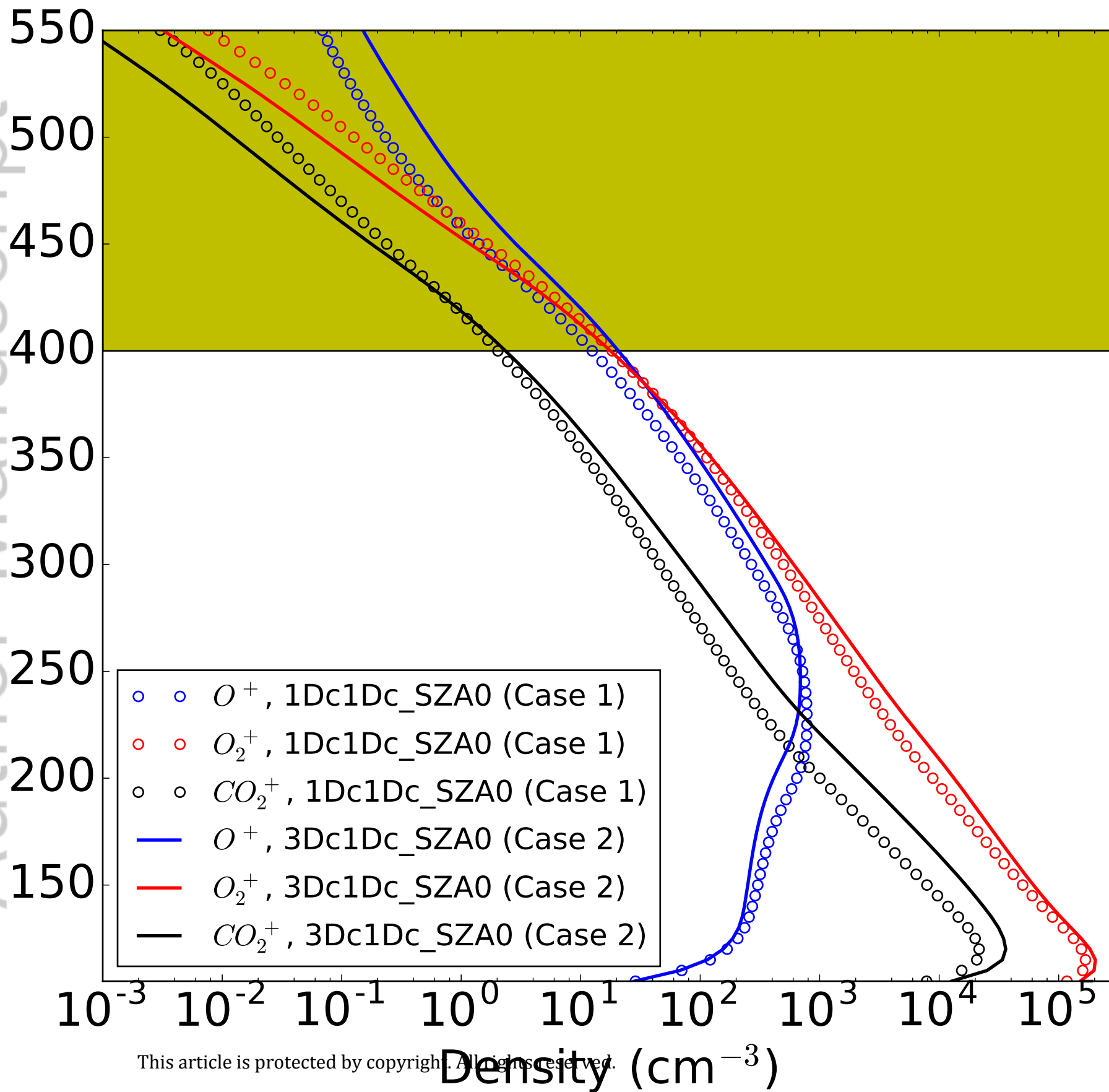


Figure 8.

Author Manuscript

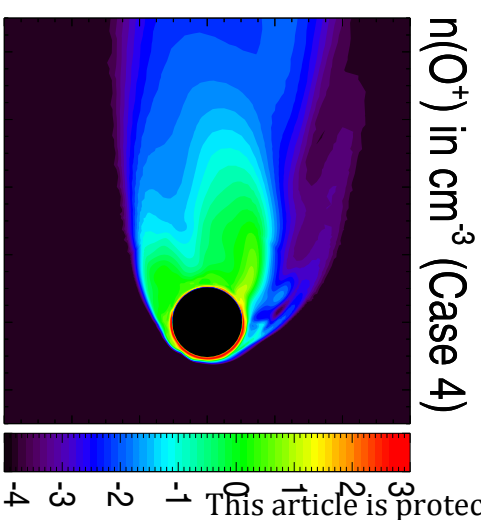
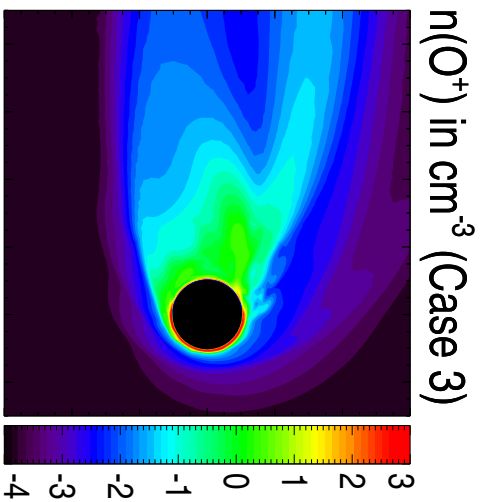
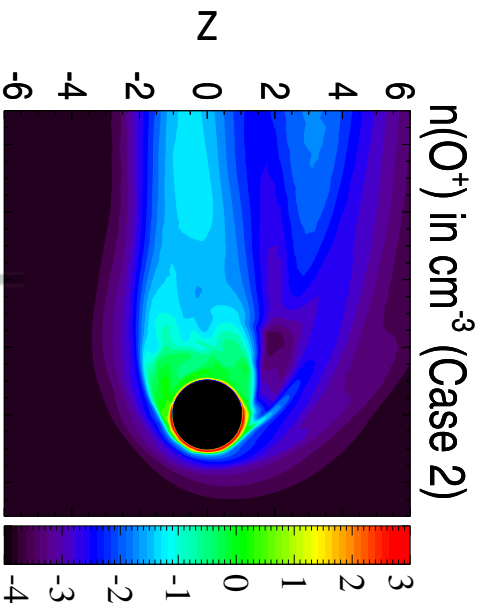




Figure 9.

Author Manuscript

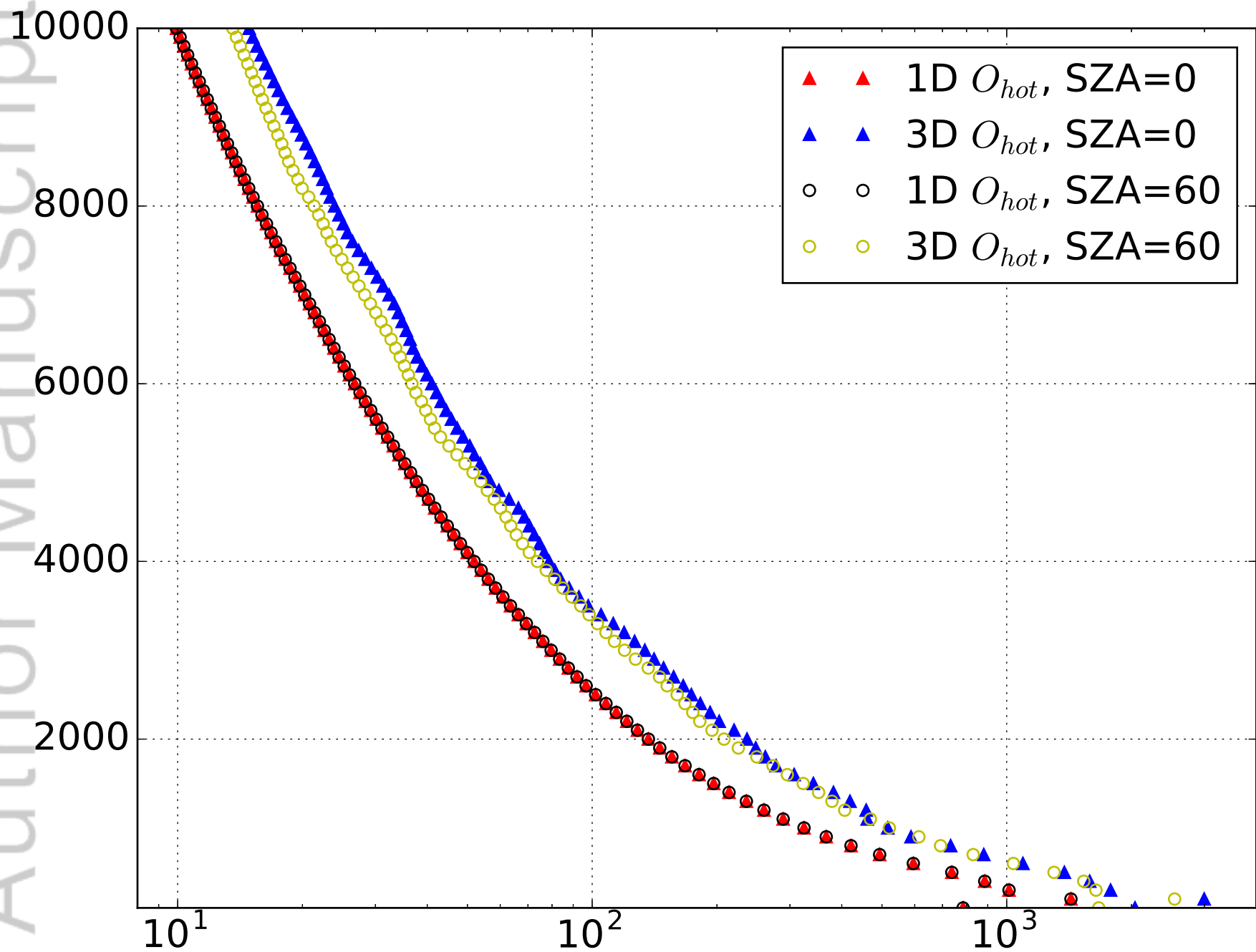
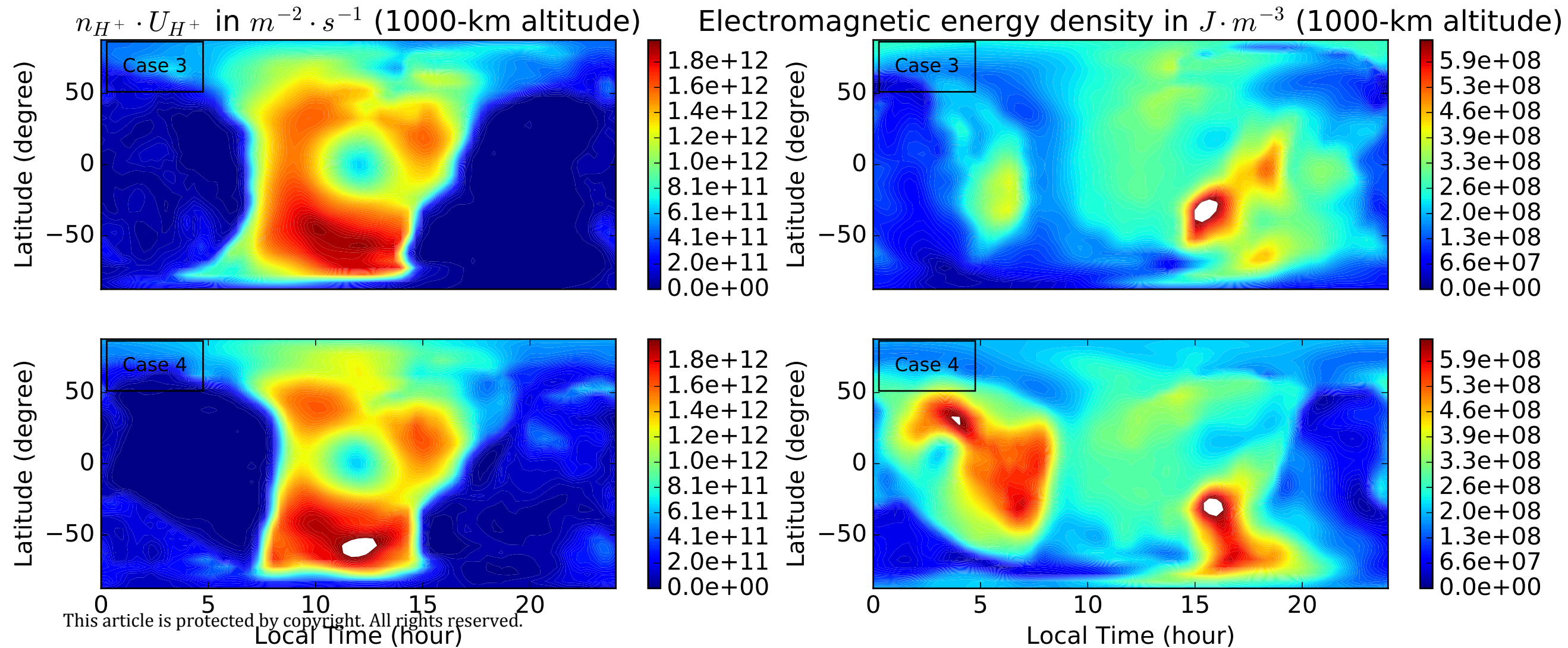


Figure 10.

Author Manuscript



# Solar wind interaction with the Martian upper atmosphere: Roles of the cold thermosphere and hot oxygen corona

Chuanfei Dong,<sup>1,2</sup> Stephen W. Bougher,<sup>3</sup> Yingjuan Ma,<sup>4</sup> Yuni Lee,<sup>5</sup> Gabor Toth,<sup>3</sup> Andrew F. Nagy,<sup>3</sup> Xiaohua Fang,<sup>6</sup> Janet Luhmann,<sup>7</sup> Michael W. Liemohn,<sup>3</sup> Jasper S. Halekas,<sup>8</sup> Valeriy Tenishev,<sup>3</sup> David J. Pawlowski,<sup>9</sup> Michael R. Combi<sup>3</sup>

<sup>1</sup>Department of Astrophysical Sciences, Princeton University, Princeton, New Jersey, USA

<sup>2</sup>Princeton Center for Heliophysics, Princeton Plasma Physics Laboratory, Princeton University, Princeton, New Jersey, USA

<sup>3</sup>Department of Climate and Space Sciences and Engineering, University of Michigan, Ann Arbor, Michigan, USA.

<sup>4</sup>Department of Earth and Space Sciences, University of California, Los Angeles, California, USA.

<sup>5</sup>NASA Goddard Space Flight Center, Greenbelt, Maryland, USA.

<sup>6</sup>Laboratory for Atmospheric and Space Physics, University of Colorado, Boulder, Colorado, USA.

<sup>7</sup>Space Sciences Laboratory, University of California, Berkeley, California, USA.

<sup>8</sup>Department of Physics and Astronomy, University of Iowa, Iowa City, Iowa, USA.

<sup>9</sup>Department of Physics and Astronomy, Eastern Michigan University, Ypsilanti, Michigan, USA.

## Key Points:

- Despite the similar ion loss rate calculated from 1D and 3D atmospheres, the latter are required to adequately reproduce MAVEN observations.
- The hot oxygen corona plays an important role in protecting the Martian ionosphere and thermosphere from the solar wind erosion.
- The thermospheric oxygen atom is the primary neutral source for O<sup>+</sup> ion escape during the relatively weak solar cycle 24.

---

Corresponding author: Chuanfei Dong, [dcfy@princeton.edu](mailto:dcfy@princeton.edu)

## Abstract

We study roles of the thermosphere and exosphere on the Martian ionospheric structure and ion escape rates in the process of the solar wind-Mars interaction. We employ a four-species multifluid MHD (MF-MHD) model to simulate the Martian ionosphere and magnetosphere. The *cold* thermosphere background is taken from the Mars Global Ionosphere Thermosphere Model (M-GITM) and the hot oxygen exosphere is adopted from the Mars exosphere Monte Carlo model - Adaptive Mesh Particle Simulator (AMPS). A total of four cases with the combination of 1D (globally averaged) and 3D thermospheres and exospheres are studied.

The ion escape rates calculated by adopting 1D and 3D atmospheres are similar; however, the latter are required to adequately reproduce MAVEN ionospheric observations. In addition, our simulations show that the 3D hot oxygen corona plays an important role in preventing planetary molecular ions ( $\text{O}_2^+$  and  $\text{CO}_2^+$ ) escaping from Mars, mainly resulting from the mass loading of the high-altitude exospheric  $\text{O}^+$  ions. The *cold* thermospheric oxygen atom, however, is demonstrated to be the primary neutral source for  $\text{O}^+$  ion escape during the relatively weak solar cycle 24.

## 1 Introduction

Unlike Earth and Venus, Mars with a relatively weak surface gravity allows an extended corona of hot oxygen that can partially escape to space [Wallis, 1978; Ip, 1988; Nagy and Cravens, 1988; Fox, 1993]. Being the most important reaction, the dissociative recombination of  $\text{O}_2^+$  (deep in the dayside thermosphere/ionosphere) is responsible for producing most of dayside exospheric hot atomic oxygen ( $\text{O}_2^+ + e \rightarrow \text{O}^* + \text{O}^*$ ), therefore, the distribution of the hot oxygen exosphere is asymmetric around the Mars globe [Vaille et al., 2009; Lee et al., 2015a]. Note that it is not only the model that shows the hot O distribution is asymmetric, but it is also seen in the MAVEN Imaging Ultraviolet Spectrograph (IUVS) data [e.g., Lee et al., 2015b; Leblanc et al., 2017]. In addition to the dissociative recombination of  $\text{O}_2^+$ , the sputtering caused by collisions between the pickup ions (e.g.,  $\text{O}^+$ ) and the Martian thermospheric background may also be an important source for the hot corona [Luhmann and Kozyra, 1991; Johnson and Luhmann, 1998; Leblanc et al., 2018]. Compared with the *cold* thermospheric background, the *hot* (or energetic) oxygen has a thermal speed,  $\langle v_O \rangle = (2k_B T_O / m_O)^{1/2}$ , higher than the local thermal speed of the thermosphere.

Besides the strong day-night asymmetry exhibited in the hot oxygen density distribution, the major neutral species in the Martian thermosphere ( $\text{CO}_2$  and O) are also distributed asymmetrically about the planet [e.g., Bougher et al., 2008; Bougher et al., 2015a]. Specifically, more neutral  $\text{CO}_2$  molecules are in the dayside thermosphere than on the nightside at a given altitude because the  $\text{CO}_2$  global distribution is mainly controlled by the global temperature instead of the dynamics. Therefore, the thermospheric  $\text{CO}_2$  density increases (decreases) on the dayside (nightside) where temperatures are higher (lower). The density distribution of atomic O (especially on the nightside), however, is mainly controlled by the day-night transport due to its relatively low mass; photochemistry may make certain contribution on the dayside oxygen density distribution. For atomic O, transport begins to have an effect as the thermospheric winds increase with increasing altitude above the region where dayside O is produced photochemically; the day-to-night atomic O distribution is impacted strongly by winds roughly above  $\sim 130$  km [Bougher et al., 2015a]. The neutral wind can transport atomic O from dayside to nightside, resulting in a bulge of neutral O in the nightside thermosphere [Bougher et al., 2015a].

In order to capture the asymmetry in the Martian thermosphere and exosphere, three-dimensional “whole atmosphere” (from the ground to the exobase, 0 to  $\sim 250$  km) [Bougher et al., 2015a] and exosphere [Lee et al., 2015a] models are ultimately required to capture these asymmetric features. The modeled thermosphere and exosphere can be further input

74 into a global plasma code as the neutral background, such that roles of the 3D thermo-  
 75 sphere and exosphere on the Martian ionospheric structure and ion escape processes can  
 76 be investigated in detail. Note that the incident solar wind at Mars encounters an extended  
 77 hot exosphere, a conductive ionosphere, and highly localized crustal magnetic fields (the  
 78 strongest of which in the southern hemisphere [Acuña *et al.*, 1999]), resulting in a complex  
 79 obstacle to the solar wind that varies on all spatial and temporal scales. Among all the ob-  
 80 jects in the solar system, Mars, therefore, offers a uniquely challenging set of conditions to  
 81 simulate.

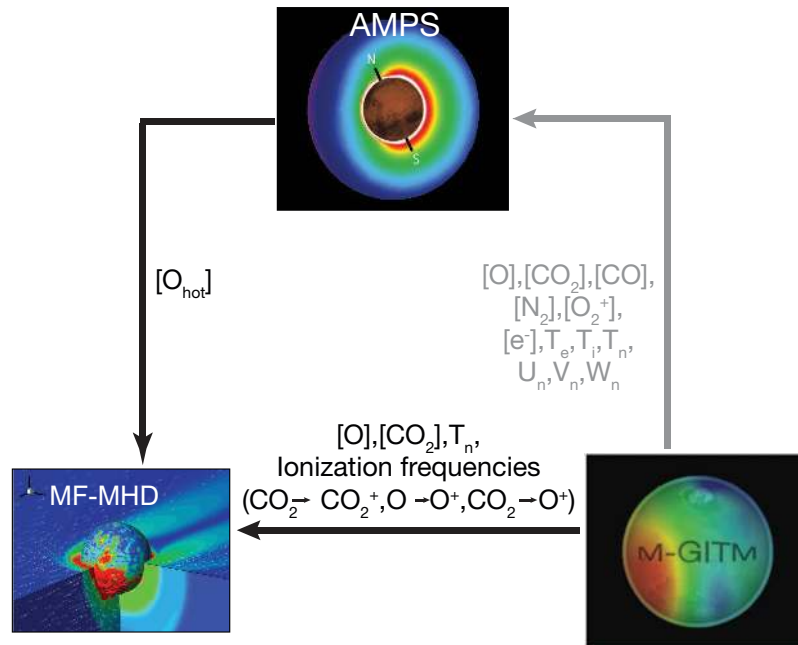
82 In recent years, investigations of the Martian thermosphere/ionosphere structure  
 83 [e.g., Withers *et al.*, 2015; Bougher *et al.*, 2015b], magnetic topology [e.g., Luhmann *et al.*,  
 84 2015; Xu *et al.*, 2016; Liemohn *et al.*, 2017; DiBraccio *et al.*, 2018], and atmospheric ion  
 85 escape rates [e.g., Halekas *et al.*, 2016; Fang *et al.*, 2017; Egan *et al.*, 2018] have become  
 86 increasingly important because they are closely related to the evolution of the Martian at-  
 87 mosphere and can affect its climate over the past four billion years [e.g., Jakosky *et al.*,  
 88 2015a; Bougher *et al.*, 2015c; Lillis *et al.*, 2015, and the references therein]. In-situ space-  
 89 craft measurements [e.g., Lundin *et al.*, 2013; Ramstad *et al.*, 2015; Dong *et al.*, 2015c;  
 90 Brain *et al.*, 2015] have greatly improved our estimates of global ion loss rates at the cur-  
 91 rent epoch. By using Mars Express (MEX) Analyzer of Space Plasmas and Energetic  
 92 Atoms 3 (ASPERA-3) data from June 2007 to January 2013, Lundin *et al.* [2013] reported  
 93 that the average heavy ion escape rate increased approximately by a factor of 10, from  
 94  $1 \times 10^{24} \text{ s}^{-1}$  (solar minimum) to  $1 \times 10^{25} \text{ s}^{-1}$  (solar maximum). More recently, Brain  
 95 *et al.* [2015] analyzed four months of Mars Atmosphere and Volatile Evolution (MAVEN)  
 96 spacecraft data and estimated a net ion escape rate of  $\sim 2.5 \times 10^{24} \text{ s}^{-1}$  by choosing a  
 97 spherical shell at  $\sim 1000$  km above the planet with energies  $> 25$  eV during solar cycle  
 98 maximum conditions. In addition, Liemohn *et al.* [2014] and Dong *et al.* [2015c] con-  
 99 firmed the substantial plume-like distribution of escaping ions from the Martian atmo-  
 100 sphere in MEX and MAVEN observations, organized by the upstream solar wind convec-  
 101 tion electric field. It is also worth noting that the total ion loss rate increased by more  
 102 than one order of magnitude during an interplanetary corona mass ejection (ICME) event  
 103 observed by MAVEN on March 8th, 2015 [Jakosky *et al.*, 2015b; Dong *et al.*, 2015b; Curry  
 104 *et al.*, 2015b; Ma *et al.*, 2017; Luhmann *et al.*, 2017]. Moreover, Lingam *et al.* [2018] found  
 105 that the solar energetic protons (SEPs) associated with extreme space weather events with  
 106 energies  $\gtrsim 150$  MeV can reach the Martian surface; the same cutoff value has also been  
 107 presented by the Mars Science Laboratory's Curiosity rover group [Hassler *et al.*, 2014].

108 In order to study the solar wind interaction with the Martian upper atmosphere, var-  
 109 ious plasma fluid models and kinetic particle codes have been developed. A few notable  
 110 examples include the multi-species single-fluid MHD models [Ma *et al.*, 2004, 2014], the  
 111 multifluid MHD models [Harnett and Winglee, 2006; Najib *et al.*, 2011; Rioussset *et al.*,  
 112 2013, 2014; Dong *et al.*, 2014a, 2015a], the test-particle approach [Fang *et al.*, 2008, 2010a;  
 113 Curry *et al.*, 2014, 2015a] and the hybrid particle-in-cell (hybrid-PIC) codes [Modolo  
 114 *et al.*, 2016; Brecht *et al.*, 2016]. These codes have been used to help quantify the ion es-  
 115 cape rates from the Martian upper atmosphere through the solar wind-Mars interaction.  
 116 Most of these studies can reach a reasonable agreement with the spacecraft observations.  
 117 However, until now no systematic study was focused on the influence of 3D thermospheres  
 118 and exospheres on the Martian ionospheric structure and ion escape rates.

119 In this paper, we adopt the 3D Mars thermosphere (i.e., neutral temperatures  $T_n$ ,  
 120 neutral densities  $n_O$ ,  $n_{CO_2}$ , and photoionization frequencies  $I_O$ ,  $I_{CO_2}$ ) from the Mars Global  
 121 Ionosphere Thermosphere Model (M-GITM) [Bougher *et al.*, 2015a] and the hot atomic  
 122 oxygen density,  $n_{O_{hot}}$ , from the Mars exosphere Monte Carlo model - Adaptive Mesh  
 123 Particle Simulator (AMPS) [Lee *et al.*, 2015a]. M-GITM and Mars AMPS are one-way  
 124 coupled with the 3D Block-Adaptive-Tree-Solarwind-Roe-Upwind-Scheme (BATS-R-US)  
 125 Mars multifluid MHD (MF-MHD) model [Najib *et al.*, 2011; Dong *et al.*, 2014a, 2015a]  
 126 (see Figure 1 for the one-way coupled framework). The Mars AMPS hot oxygen corona

127 is calculated based on the thermosphere/ionosphere background from M-GITM [Lee *et al.*,  
 128 2015a]. In the present work, the simulations are carried out for four selected cases with  
 129 the combination of 1D and 3D neutral atmospheres.

130 The remainder of this paper is divided into three sections. In Section 2, we briefly  
 131 introduce the three models employed in this study. In Section 3.1, we investigate the role  
 132 of the 3D thermosphere on the Martian ionospheric structure and ion escape rates by  
 133 means of data-model and model-model comparisons. In Section 3.2, we study the effect  
 134 of the 3D exosphere on the ion escape rate and the corresponding molecular to atomic  
 135 escaping ion ratio  $(O_2^+ + CO_2^+)/O^+$  through model-model comparisons. Discussion and Con-  
 136 clusions are summarized in the last section.



137 **Figure 1.** Sketch of a one-way coupling approach between M-GITM, Mars AMPS and MF-MHD (after  
 138 Figure 1 of Dong *et al.* [2015a]). The notation  $T_n$  denotes the neutral atmospheric temperature. The quan-  
 139 tities  $[O]$ ,  $[CO_2]$ , and  $[O_{hot}]$  are the thermospheric *cold* O,  $CO_2$  and exospheric *hot* O number densities,  
 140 respectively. In this study, we adopt the one-way coupling indicated by the solid black lines. For the detailed  
 141 study of the one-way coupling between M-GITM and Mars AMPS (solid gray line), please refer to Lee *et al.*  
 142 [2015a].

## 143 2 Model Description

144 In this section, M-GITM, AMPS, and MF-MHD are briefly introduced. All these  
 145 models have been adopted to support the MAVEN mission activities (2014-2018).

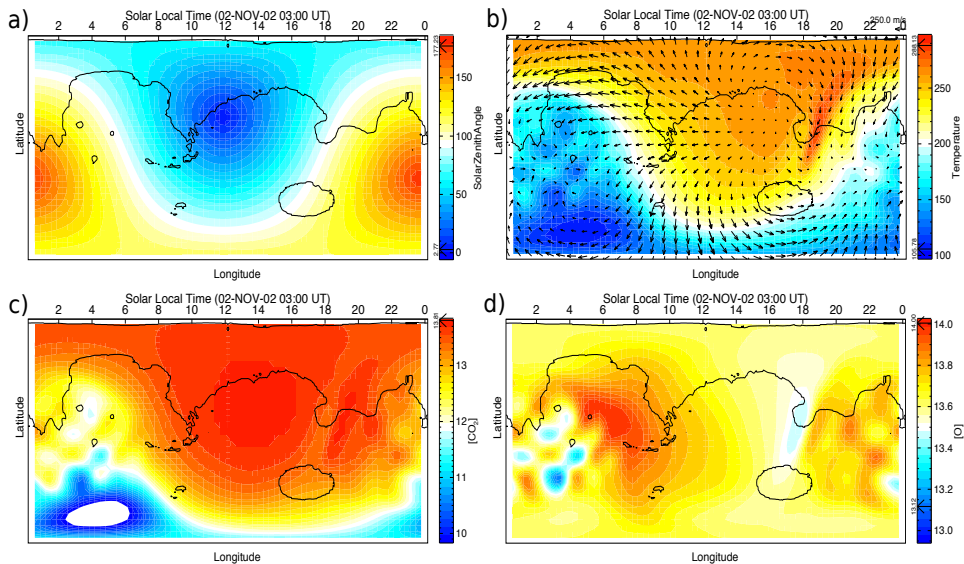
### 146 2.1 Mars Global Ionosphere Thermosphere Model (M-GITM)

147 Mars Global Ionosphere Thermosphere Model (M-GITM) [Bougher *et al.*, 2015a],  
 148 combines the terrestrial GITM framework [Ridley *et al.*, 2006; Deng *et al.*, 2008] with  
 149 the fundamental physical parameters, ion-neutral chemistry, and key radiative processes  
 150 for Mars in order to capture the basic observed features of the thermal, compositional,  
 151 and dynamical structure of the Mars atmosphere from the ground to the exobase (0 – 250



152 km). M-GITM currently solves for three-dimensional neutral and ion densities, as well as  
 153 neutral temperatures and winds around the globe. Key neutral species presently include:  
 154 CO<sub>2</sub>, CO, O, N<sub>2</sub>, O<sub>2</sub>, Ar, and He. Five key photochemical ion species currently include:  
 155 O<sup>+</sup>, O<sub>2</sub><sup>+</sup>, CO<sub>2</sub><sup>+</sup>, N<sub>2</sub><sup>+</sup> and NO<sup>+</sup>. Typically, production runs are conducted for a 5 × 5 degree  
 156 longitude-latitude grid, with a constant 2.5 km vertical resolution (~ 0.25 scale height,  
 157  $H_s = k_B T / mg$ , where  $k_B$  is Boltzmann constant,  $g$  is the acceleration due to planetary  
 158 gravity,  $T$  is the neutral temperature, and  $m$  is the mass of the neutral species).

159 M-GITM validation studies thus far have focused upon simulations for a range of  
 160 solar cycles and seasonal conditions [Bougher *et al.*, 2015a,b, 2017]. Figure 2a shows the  
 161 solar zenith angle (SZA) distribution around Mars' globe for aphelion solar moderate  
 162 conditions (APHMOD) in the Geographic (GEO) coordinate system. The subsolar point (i.e.,  
 163 where SZA=0) is located in the northern hemisphere. An inspection of Figure 2b reveals  
 164 that solar-driven exobase temperatures peak in the middle afternoon at the subsolar lati-  
 165 tude (25°N). The warmer temperature near the evening terminator (LT = 18) is a result  
 166 of the dynamical heating due to the convergent zonal winds [Bougher *et al.*, 2015a]. The  
 167 asymmetric distribution of CO<sub>2</sub> in latitude (Figure 2c) is closely related to the asymmetric  
 168 diurnal temperature distribution (Figure 2b). Conversely, Figure 2d presents atomic oxygen  
 169 density distributions for which dayside-produced O is transported to the nightside by  
 170 the thermospheric wind system, where it subsequently accumulates at low-to-middle latitudes  
 171 around LT = 4–8. All the features shown in Figure 2 indicate the importance of adopting  
 172 the 3D M-GITM thermosphere in a global plasma model in order to reproduce the iono-  
 173 spheric structure and accurately estimate the ion escape rates in the process of the solar  
 174 wind-Mars interaction.



175 **Figure 2.** The color contours of (a) solar zenith angle (SZA, in degree), (b) Temperature (in K), (c) log<sub>10</sub>  
 176 CO<sub>2</sub> densities (in m<sup>-3</sup>), and (d) log<sub>10</sub> atomic O densities (in m<sup>-3</sup>) at ~ 200 km (exobase) altitude for aphelion  
 177 solar moderate conditions (APHMOD, Ls=90, F<sub>10.7</sub>=130). The arrows in Figure 2 (b) indicate the relative  
 178 magnitude and the direction of the horizontal winds. All the vertical axes (i.e., latitude) range from -90° to  
 179 90°. The white color highlights the regions below the low saturation of the colorbar.

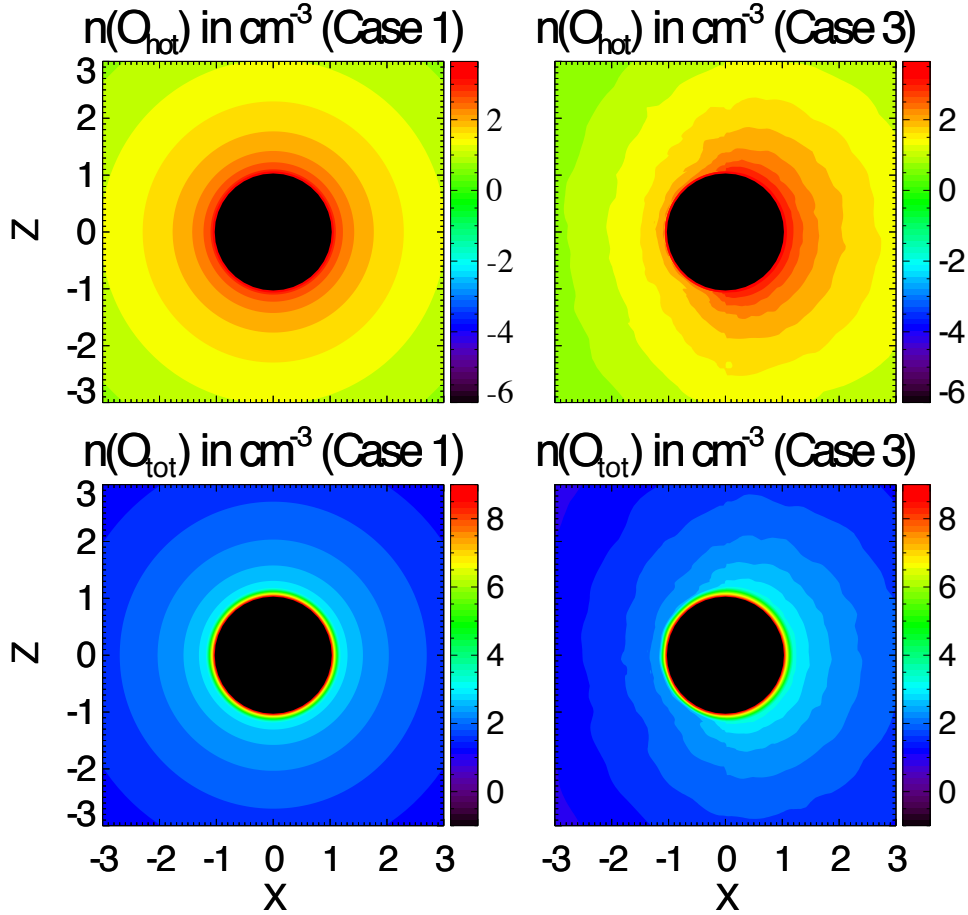
## 2.2 Mars Adaptive Mesh Particle Simulator (AMPS)

The code we employ to model the Martian exosphere is the 3D Mars Adaptive Mesh Particle Simulator (AMPS), which runs in the test-particle mode using the Direct Simulation Monte Carlo (DSMC) method [Bird, 1994]. The AMPS code [Tenishev and Combi, 2008; Tenishev et al., 2013a; Lee et al., 2015a] is a well-tested code for a wide range of kinetic problems in rarefied gas regime. Examples of the AMPS applications include the cometary coma and the exospheres of Mars, Mercury and the Moon. The 3D structure and photochemical loss of hot oxygen particles from Mars have been investigated by taking advantage of the one-way coupled framework between Mars AMPS and M-GITM [Lee et al., 2015a,b]. As shown in Figure 1, AMPS calculates the hot atomic oxygen density distribution based on the thermospheric background (i.e., neutral species O, CO<sub>2</sub>, N<sub>2</sub>, CO) from M-GITM.

Compared with the previous version where it assumed idealized hard sphere collisions and only isotropic scattering in the center of mass frame [Vaille et al., 2009], the current AMPS considers a more realistic description for the collisions between hot O and ambient species by adopting a forward scattering collision scheme with the angular differential scattering cross sections from Kharchenko et al. [2000]. The related integrated cross sections (in cm<sup>2</sup>) are  $1.2 \times 10^{-14}$  for O-CO<sub>2</sub>,  $6.4 \times 10^{-15}$  for O-O, and  $1.8 \times 10^{-14}$  for both O-N<sub>2</sub> and O-CO. The current AMPS (by adopting the forward scattering scheme) produces a more intensive (and closer to observed) hot oxygen corona than the previous case by adopting the isotropic scattering scheme, and thus enhances the corresponding photochemical escape rate [Lee et al., 2015a]. However, there still exists certain discrepancy between MAVEN observations and AMPS predictions [Lee et al., 2015a]; further improvement of model predications of hot oxygen corona is an ongoing MAVEN effort.

The motion of each hot particle is influenced by the gravitational field of the Mars and modified by collisions with the background thermospheric species. The collision in the code depends on the rate of change in the background densities (i.e., rate of change in collision frequency). Although the nominal cell size is about 60 km at the model lower boundary (at 100 km altitude above the Martian surface), the large grid size does not prevent AMPS from capturing the variation in the Martian ionosphere and thermosphere. In AMPS, each macro-particle is initialized based on the thermospheric background prescribed by M-GITM (stored in an additional data table) at its resolution. It is noteworthy that the hybrid-PIC codes [e.g., Modolo et al., 2016; Brecht et al., 2016] have similar grid resolution for studying the solar-wind Mars interaction. The AMPS computational domain extends to 6 Mars radius (one Mars radius,  $R_M \sim 3396$  km).

Figure 3 illustrates the hot and total (the sum of thermal and hot components) atomic oxygen distribution around the Mars globe in a logarithmic scale. Figure 3 is based on the Mars-centered Solar Orbital (MSO) coordinate system, where the +X axis points from Mars to the Sun, the +Z axis is perpendicular to the Martian orbital plane and points northward, and the Y axis completes the right-hand system. The left panels correspond to the global hot and total O distribution of the 1D spherically symmetric case, i.e., by averaging over all the longitudes and latitudes from the 3D AMPS output,  $\bar{n}(r) = \frac{\int_0^\pi \int_0^{2\pi} n(r, \theta, \phi) \sin \theta d\theta d\phi}{\int_0^\pi \int_0^{2\pi} \sin \theta d\theta d\phi}$ . The right panels show the original 3D AMPS and M-GITM output. An inspection of the second row of Figure 3 reveals that the thermal atomic oxygen dominates over the hot component at relatively low altitudes (i.e., in the thermosphere), while the hot atomic oxygen is the dominant neutral species at relatively high altitudes (i.e., in the exosphere). Both panels are for the aphelion solar moderate conditions (APHMOD). The 3D AMPS hot oxygen corona shows a great day-night asymmetry which cannot be captured by a 1D spherically symmetric profile. The remarkable asymmetry shown in Figure 3 indicates the significance of adopting the 3D hot oxygen corona in a global plasma code for studying the Martian atmospheric ion loss.



231 **Figure 3.** Comparisons of the hot atomic oxygen (first row) and total atomic oxygen (the sum of thermal  
 232 and hot component, second row) density distribution (in  $\text{cm}^{-3}$ ) from the globally averaged 1D spherically  
 233 symmetric AMPS profile (left) and the 3D profile (right) in the x-z meridian plane in the MSO coordinate  
 234 system. Both cases are based on the aphelion solar moderate conditions (APHMOD). Note the use of different  
 235 logarithmic scales.

### 236 2.3 BATS-R-US Mars multifluid MHD (MF-MHD) Model

237 The 3D BATS-R-US multifluid MHD (MF-MHD) model solves separate continuity,  
 238 momentum and energy equations for each fluid [Powell *et al.*, 1999; Glocer *et al.*, 2009;  
 239 Najib *et al.*, 2011; Tóth *et al.*, 2012; Huang *et al.*, 2016; Dong *et al.*, 2017a]. For the Mars  
 240 version, it solves MHD equations for four ion fluids  $\text{H}^+$ ,  $\text{O}^+$ ,  $\text{O}_2^+$ ,  $\text{CO}_2^+$  [Najib *et al.*, 2011;  
 241 Dong *et al.*, 2014a, 2015a]. Interestingly, Rubin *et al.* [2014] showed that by using a multi-  
 242 fluid MHD model, it can mimic some major features obtained with the hybrid-PIC calcu-  
 243 lation for a weak comet, such as the finite gyration effect of the planetary/cometary  
 244 heavy ions and the associated pickup processes. The underlying reason is that MF-MHD  
 245 includes the dynamics of individual ion species. The Lorentz force term,  $\propto (\mathbf{u}_s - \mathbf{u}_+) \times \mathbf{B}$ ,  
 246 in the individual ion momentum equation is mainly responsible for the asymmetric ion es-  
 247 cape plume and the associated pickup processes, resulting from the difference between the  
 248 charge averaged ion velocity,  $\mathbf{u}_+$ , and the individual fluid velocity,  $\mathbf{u}_s$ , of species  $s$  [Dong  
 249 *et al.*, 2014a].

254 At the MF-MHD model lower boundary (100 km above the Martian surface), the  
 255 densities of  $\text{O}^+$ ,  $\text{O}_2^+$ ,  $\text{CO}_2^+$  satisfy the photochemical equilibrium condition [e.g. Schunk

250 **Table 1.** Chemical reactions and associated rates in Mars multifluid MHD code. The ion-neutral and ion-  
 251 electron chemical reaction rates are adopted from *Najib et al.* [2011], while the photoionization frequencies  
 252 (at the top of atmosphere for aphelion solar moderate conditions) are adopted from *Bougher et al.* [2015a] as  
 253 indicated in Figure 1.

Chemical Reaction	Rate (s <sup>-1</sup> )
Primary Photolysis and Particle Impact	
$\text{CO}_2 + h\nu \rightarrow \text{CO}_2^+ + e^-$	$8.37 \times 10^{-7}$
$\text{CO}_2 + h\nu \rightarrow \text{CO} + \text{O}^+ + e^-$	$7.52 \times 10^{-8}$
$\text{O} + h\nu \rightarrow \text{O}^+ + e^-$	$1.52 \times 10^{-7}$
$\text{H} + h\nu \rightarrow \text{H}^+ + e^-$	$5.58 \times 10^{-8}$
$e^- + \text{H} \rightarrow e^- + \text{H}^+ + e^-$	see text
$e^- + \text{O} \rightarrow e^- + \text{O}^+ + e^-$	see text
Ion-Neutral Chemistry	
$\text{CO}_2^+ + \text{O} \rightarrow \text{O}_2^+ + \text{CO}$	$1.64 \times 10^{-10}$
$\text{CO}_2^+ + \text{O} \rightarrow \text{O}^+ + \text{CO}_2$	$9.60 \times 10^{-11}$
$\text{O}^+ + \text{CO}_2 \rightarrow \text{O}_2^+ + \text{CO}$	$1.1 \times 10^{-9} (800/T_i)^{0.39}$
$\text{O}^+ + \text{H} \rightarrow \text{H}^+ + \text{O}$	$6.4 \times 10^{-10}$
$\text{H}^+ + \text{O} \rightarrow \text{O}^+ + \text{H}$	$5.08 \times 10^{-10}$
Ion-Electron Recombination Chemistry	
$\text{O}_2^+ + e^- \rightarrow \text{O} + \text{O}$	$7.38 \times 10^{-8} (1200/T_e)^{0.56}$
$\text{CO}_2^+ + e^- \rightarrow \text{CO} + \text{O}$	$3.10 \times 10^{-7} (300/T_e)^{0.5}$

256 *and Nagy*, 2009, chapters 8 and 13]. A reflective inner boundary condition for the ve-  
 257 locity  $\mathbf{u}$  is used, which leads to an approximately zero velocity at the inner boundary as  
 258 expected. The plasma temperature is set to be twice the value of the neutral temperature  
 259 at the inner boundary, where both ions and electrons have roughly the same temperature  
 260 as neutrals due to collisions. We use the 60 degree harmonic expansion model of *Arkani-*  
 261 *Hamed* [2001] to describe the crustal magnetic fields at Mars [*Acuña et al.*, 1999]. The  
 262 photochemical reactions in the model include charge exchange, photoionization, electron  
 263 impact ionization and ion-electron recombination. The electron impact ionization rates are  
 264 given by *Cravens et al.* [1987]. The elastic collision frequencies are taken from *Schunk*  
 265 *and Nagy* [2009]. Table 1 summarizes the chemical reactions and the associated rates for  
 266 inelastic collisions used in the multifluid MHD calculations.

267 The smallest radial resolution is about 5 km at the inner boundary while the grid  
 268 size can increase to several thousand kilometers at the outer boundary ( $\sim 30 R_M$ ) due to  
 269 the nonuniformity in the mesh design. The angular resolution varies from  $1.5^\circ$  to  $3.0^\circ$   
 270 in a spherical grid mesh bounded by a cube with  $-30R_M \leq X \leq 8R_M$ ;  $-30R_M \leq Y, Z \leq$   
 271  $30R_M$ .

### 272 3 Simulation Results and Discussion

273 In this section, we discuss the simulation results obtained by using the one-way cou-  
 274 pling approach, i.e., both the M-GITM and AMPS neutral profiles are used as the inputs  
 275 for the MF-MHD model (Figure 1). Firstly, in order to study the effect of the 3D thermo-  
 276 sphere on the Martian ionospheric structure and ion escape rates, we adopt either the 1D  
 277 globally averaged (and thus spherically symmetric) thermosphere (Case 1) or the 3D M-

286 **Table 2.** Input parameters used for different cases. The solar cycle conditions are chosen based upon one  
 287 MAVEN trajectory (orbit O2349) on 2015-12-14, during which it has a dayside periapsis.

Simulation #	Subsolar Position of Periapsis	Neutral Atmosphere	Solar Cycle Conditions
Case 1	167.9°E, 24.9°N	1D <sub>cold</sub> and 1D <sub>hot</sub>	Aphelion Solar
Case 2	167.9°E, 24.9°N	3D <sub>cold</sub> and 1D <sub>hot</sub>	Moderate
Case 3	167.9°E, 24.9°N	3D <sub>cold</sub> and 3D <sub>hot</sub>	(APHMOD)
Case 4	167.9°E, 24.9°N	3D <sub>cold</sub> without O <sub>hot</sub>	

288 **Table 3.** Solar wind input parameters used for different cases. The solar wind inputs are taken from  
 289 MAVEN measurements on 2015-12-14 (orbit O2349), during which it has a steady solar wind and IMF.

Simulation #	$n_{sw}$ (cm <sup>-3</sup> )	$v_{sw}$ (km/s)	IMF (nT)	$T_{sw}^{proton}$ & $T_{sw}^{electron}$ (K)
Cases 1-4	4.85	(-348.5, -7.0, -25.5)	(-0.25, 5.5, -1.0)	$5.9 \times 10^4$ & $1.3 \times 10^5$

290 **Table 4.** Calculated ion escape rates (in  $\times 10^{24}$  s<sup>-1</sup>) and molecular to atomic escaping ion ratio listed in the  
 291 last column.

Simulation cases	O <sup>+</sup>	O <sub>2</sub> <sup>+</sup>	CO <sub>2</sub> <sup>+</sup>	Total	(O <sub>2</sub> <sup>+</sup> + CO <sub>2</sub> <sup>+</sup> )/O <sup>+</sup>
Case 1 (1D <sub>cold</sub> and 1D <sub>hot</sub> )	0.57	1.45	0.29	2.30	3.06
Case 2 (3D <sub>cold</sub> and 1D <sub>hot</sub> )	0.74	1.27	0.27	2.28	2.09
Case 3 (3D <sub>cold</sub> and 3D <sub>hot</sub> )	0.89	1.18	0.31	2.38	1.67
Case 4 (3D <sub>cold</sub> and noO <sub>hot</sub> )	0.88	1.52	0.40	2.80	2.17

278 GITM thermosphere (Case 2) while fixing the 1D globally averaged hot oxygen corona.  
 279 Detailed data-model comparisons along a selected MAVEN trajectory on December 14,  
 280 2015 (orbit O2349) are studied. As an illustrative example, we also present the global  
 281 ionospheric ion distribution at a constant altitude, 200 km, for both Cases 1 and 2. In Sec-  
 282 tion 3.2, we investigate the role of the 3D exosphere on the ion escape rate. Three cases  
 283 are studied for the aphelion solar moderate conditions (APHMOD) with a 1D corona, a  
 284 3D corona, and a case without a hot oxygen corona (Cases 2-4). Tables 2-3 summarize  
 285 the parameters used for each case. The ion escape rates are summarized in Table 4.

### 3.1 Effects of 3D Thermosphere on the Solar Wind-Mars Interaction

292  
 293 We first focus on the effect of the 3D thermosphere on the solar wind-Mars inter-  
 294 action. Figure 4 presents the data-model comparison of the ionospheric density profiles  
 295 between the MF-MHD calculations (dashed lines) and the MAVEN data (solid lines).  
 296 The electron density was measured by the Langmuir Probe and Waves (LPW) instrument  
 297 on board the spacecraft. The O<sup>+</sup>, O<sub>2</sub><sup>+</sup> and CO<sub>2</sub><sup>+</sup> ion densities were measured by the Neu-  
 298 tral Gas and Ion Mass Spectrometer (NGIMS). Figure 4a depicts the spacecraft altitudes  
 299 (blue), latitude (black) and solar zenith angle (red) versus time along the trajectory. The  
 300 rest of the panels are the detailed data-model comparisons based on the 1D thermosphere  
 301 and exosphere (Case 1, Figure 4b), the 3D thermosphere and the 1D exosphere (Case 2,  
 302 Figure 4c), and the 3D thermosphere and exosphere (Case 3, Figure 4d), respectively. In  
 303 Figure 4, the MF-MHD model displays the maximum ionospheric ion and electron densi-  
 304 ties at the periapsis of orbit O2349 (on December 14, 2015), in good agreement with the  
 305 MAVEN observation. Both the MF-MHD calculations and the MAVEN data reveal that  
 306 O<sub>2</sub><sup>+</sup> is the dominant ion in the Martian ionosphere.

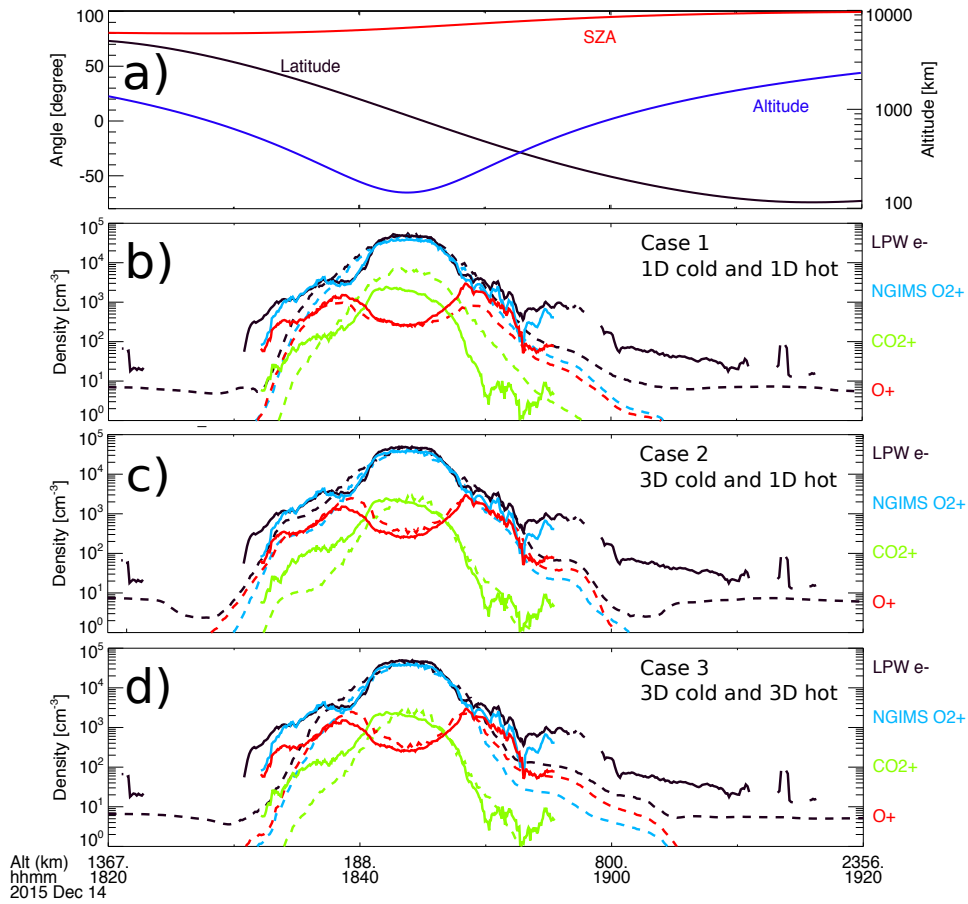
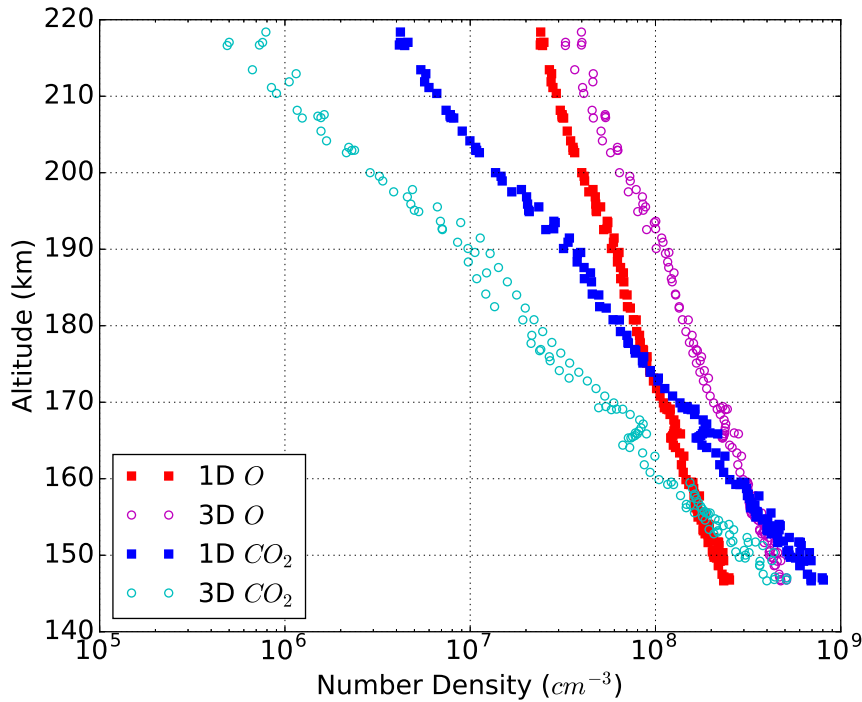


**Figure 4.** Comparisons of the ion and electron densities between the MF-MHD simulations (dashed lines) and the MAVEN observations (solid lines). The ion and electron densities are measured by NGIMS and LPW, respectively. Second panel: Case 1 with 1D thermosphere and exosphere. Third panel: Case 2 with 3D thermosphere and 1D exosphere. Fourth panel: Case 3 with 3D thermosphere and exosphere.

Compared with Case 1, the MF-MHD calculations based on the 3D M-GITM thermosphere (Case 2) fit the observational data better, demonstrating the importance of adopting the 3D thermosphere in a global plasma code. In Figure 4b, the calculated molecular ion ( $O_2^+$  and  $CO_2^+$ ) densities along the MAVEN trajectory are slightly higher than the NGIMS data whilst the  $O^+$  ion density is slightly lower than that observed. Figure 4c, however, shows an opposite trend as presented in Figure 4b. In order to understand the deviation between simulations and observations, we plot both 1D and 3D thermospheric  $O$  and  $CO_2$  densities along the MAVEN trajectory (Figure 5). As we expected, the 3D thermosphere (Case 2) has a higher  $O$  and lower  $CO_2$  abundance compared to the 1D thermosphere (Case 1) along the MAVEN trajectory. This helps to explain the variation trend in the ion densities from Figure 4b to Figure 4c. An inspection of Figure 4c and Figure 4d reveals that the 3D hot oxygen does not have a significant effect on the ionospheric density distribution compared to the 1D exosphere case.

Although we have presented the ionospheric ion densities along one MAVEN trajectory, it is also important to depict the global density distribution of the Martian ionosphere. Figures 6 illustrates the 2D (latitude vs. local time, at 200-km altitude) ionospheric maps from the MF-MHD model for Case 1 (left column) and Case 2 (right column). For both cases, the top panels show the density distribution of  $O^+$ , and the middle

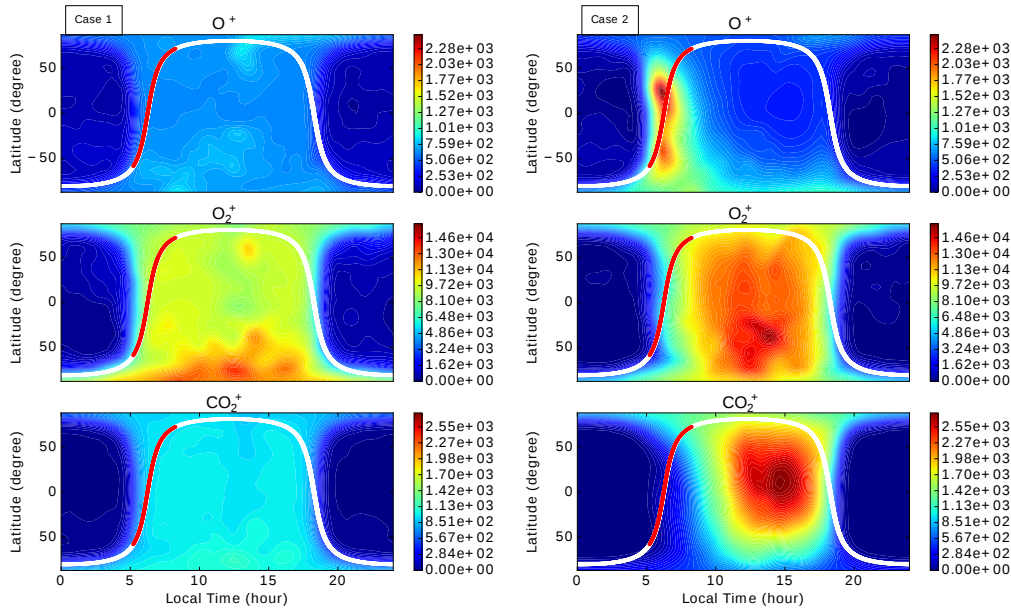


324 **Figure 5.** Comparisons between the 1D and 3D thermospheric density profiles along the MAVEN trajec-  
 325 tory. The plot includes both inbound and outbound data.

331 to bottom panels display the density distribution of  $O_2^+$  and  $CO_2^+$ , respectively. The smooth  
 332 transition of the ion density around terminator region is a result of the implementation  
 333 of Chapman function from *Smith and Smith* [1972] in the MF-MHD model. Again, both  
 334 columns show that  $O_2^+$  is the dominant ion species in the Martian ionosphere. In order  
 335 to better understand the different ion distributions shown in Figure 4, we also plotted the  
 336 projection of the MAVEN trajectory in each panel.

337 In Figure 6 (left column), all the ions mirror a similar ionospheric pattern as a re-  
 338 sult of the 1D spherically symmetric thermospheric input. The enhanced ion density in the  
 339 southern hemisphere is mainly caused by the crustal magnetic fields given that the crustal  
 340 anomalies are shifted to higher solar zenith angles (i.e. the southern polar region in MSO)  
 341 at aphelion. The same enhancement at the southernmost latitudes seen in the left column  
 342 is not present in the right column because the 3D asymmetric thermosphere (as shown in  
 343 Figure 2) produces relatively high ion abundance at lower latitudes and northern hemi-  
 344 sphere compared to the 1D thermosphere case. In Figure 6 (right column), however, the  
 345 ionospheric global distributions between molecular ions ( $O_2^+$  and  $CO_2^+$ ) and atomic ions  
 346 ( $O^+$ ) are distinct when adopting the 3D thermosphere. On the other hand,  $O_2^+$  and  $CO_2^+$   
 347 share similar ionospheric patterns. It is well known that the Martian dayside ionosphere  
 348 is triggered by the photoionization resulting from the solar EUV radiation [*Bougher et al.*,  
 349 2008]. Subsequently, the photoionized  $CO_2^+$  quickly reacts with neutral O to produce the  
 350 major ionospheric species  $O_2^+$ ; therefore,  $O_2^+$  exhibits a similar ionospheric distribution  
 351 as  $CO_2^+$ . The ionospheric density peaks of  $O_2^+$  and  $CO_2^+$  are also located at almost the  
 352 identical altitude (e.g., see Figure 7). Although thermospheric O can be photoionized by  
 353 photons (the main channel), ionized through charge exchange with other ion species, and  
 354 impact ionized by electrons to produce  $O^+$ , the absence of the neutral oxygen atom (in the

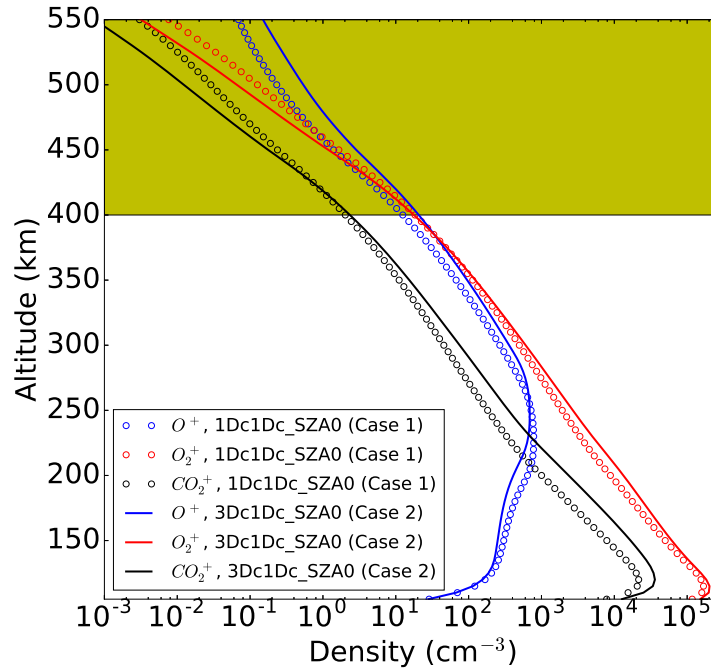
355 dayside thermosphere in 3D case) leads to a low abundance of  $O^+$  in the dayside iono-  
 356 sphere (right column of Figures 6), consistent with the neutral density distribution shown  
 357 in Figure 2. Compared with the previous work,  $O^+$  in the present work can also be pro-  
 358 duced through photoionization of  $CO_2$  as a secondary channel.



359 **Figure 6.** The ionospheric density maps for  $O^+$ ,  $O_2^+$ , and  $CO_2^+$  at 200-km altitude for Case 1 (left col-  
 360 umn) and Case 2 (right column). The thick white curve in each panel represents the projection of a selected  
 361 MAVEN trajectory (orbit O2349 on December 14, 2015). The red segment corresponds to the regions with  
 362 altitudes lower than 1000 km, including the periapsis. Note the use of different colorbar range in different  
 363 rows.

364 In order to understand the effect of the 3D thermosphere on the ion escape, we cal-  
 365 culate the ion escape rates and list them in Table 4. The calculations are conducted by  
 366 integrals of the plasma density multiplied by the radial velocity component at the surface  
 367 of a sphere far from the planet. Calculations (not presented here for the sake of brevity)  
 368 show that ion escape rates do not change to any significant degree ( $< \sim 5\%$ ) once the ra-  
 369 dius exceeds  $5 R_M$ , the result presented in the remainder of this paper use the integral  
 370 sphere with radius  $6 R_M$ . Compared with Case 1 (with 1D globally averaged thermo-  
 371 sphere), the  $O^+$  ion escape rate in Case 2 (with 3D thermosphere) increases whilst molec-  
 372 ular ionospheric ion ( $O_2^+$  and  $CO_2^+$ ) escape rate decreases. These trends can be explained  
 373 by the vertical ionospheric density profiles (at  $SZA=0$ ) shown in Figure 7. As seen from  
 374 Figure 7, more  $O^+$  at lower altitudes for Case 1 and more molecular ionospheric ions ( $O_2^+$   
 375 and  $CO_2^+$ ) at lower altitudes for Case 2, consistent with Figure 6. The relative abundance,  
 376 however, shows a contrary trend at high altitudes (in the yellow shading region). Inter-  
 377 estingly, the high-altitude ion abundance is consistent with the ion escape rates listed in  
 378 Table 4 since only those ions above a certain altitude (i.e., ion exobase) are able to escape  
 379 [e.g., *Cravens et al.*, 2017]. From test-particle simulations, *Fang et al.* [2010b] also found  
 380 that generally on the dayside, only less than 35% of ions are able to escape below 400-km  
 381 altitude.





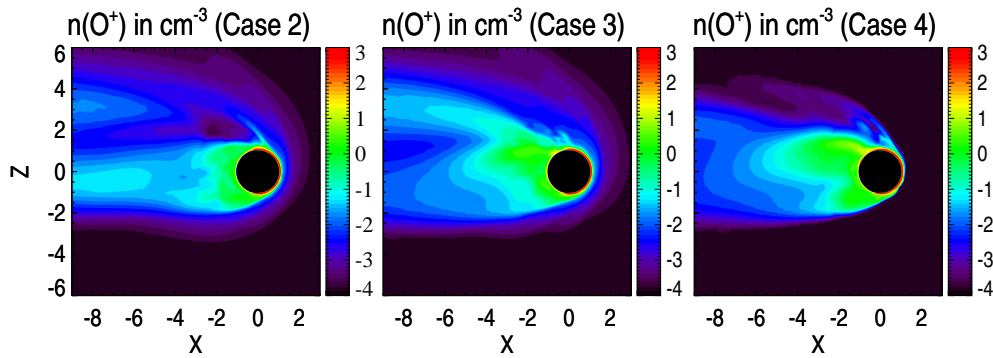
382 **Figure 7.** The vertical ionospheric density profiles for  $O^+$ ,  $O_2^+$ , and  $CO_2^+$  at SZA=0 for Case 1 (circle  
 383 markers) and Case 2 (solid curves). The yellow shading highlights a region that is more relevant to the ion  
 384 escape.

### 385 3.2 Effects of 3D Exosphere on the Solar Wind-Mars Interaction

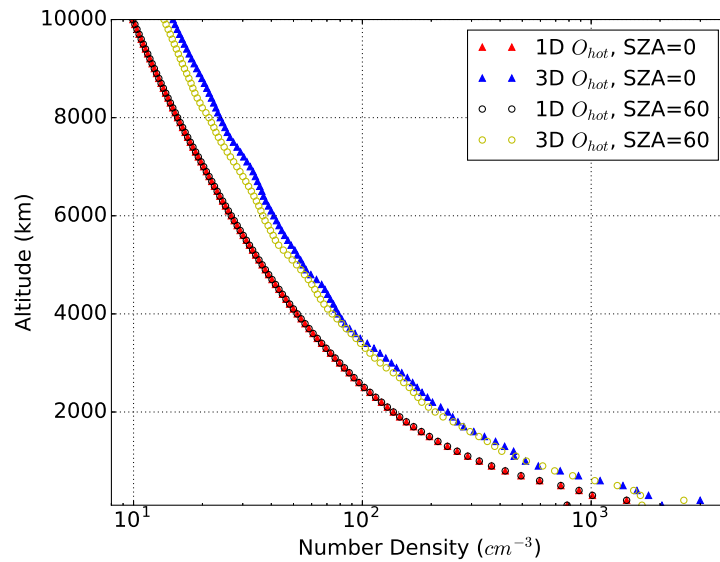
386 In order to investigate the effect of the 3D exosphere (i.e., hot oxygen corona) on the  
 387 interplay between the Martian upper atmosphere and the solar wind, we study three cases  
 388 with a 1D corona, a 3D corona, and a case without a hot oxygen corona (Cases 2-4). This  
 389 is similar to the study by *Curry et al.* [2013b], who conducted test-particle simulations to  
 390 study  $O^+$  ion loss rates with and without the 1D hot oxygen corona from *Kim et al.* [1998]  
 391 by fixing the 1D thermosphere from *Ma et al.* [2004].

#### 392 3.2.1 Effects of 3D Hot Oxygen Corona on $O^+$ Ion Escape

393 Figure 8 depicts the  $O^+$  density in the  $x$ - $z$  plane. One of the features of the MF-  
 394 MHD model is that it can capture the asymmetric escape plume of the planetary pickup  
 395 ions [*Najib et al.*, 2011; *Dong et al.*, 2014a; *Rubin et al.*, 2014]. Both Cases 2 and 3 present  
 396 dayside pickup  $O^+$  ion escaping from the extended hot oxygen corona region whilst the  
 397 high-altitude corona  $O^+$  ions cannot be observed in Case 4 due to the absence of an atomic  
 398 oxygen source. Compared with Case 2, more  $O^+$  are present in the dayside exospheric re-  
 399 gion in Case 3, consistent with those hot oxygen density distributions shown in Figure  
 400 9. All three cases present a large number of  $O^+$  ions escaping from the nightside plasma  
 401 wake region as well. The color contours in Figure 8 can be used to explain why the  $O^+$   
 402 ion escape rate of Case 2 is smallest among three cases and  $O^+$  ion escape rates between  
 403 Case 3 and Case 4 are similar. The similar ion escape rate between Case 3 and Case 4  
 404 implies that the thermospheric oxygen atoms make a significant contribution on the  $O^+$   
 405 ion escape rate.



406 **Figure 8.** Comparisons of  $O^+$  density in the  $x$ - $z$  plane for a 1D corona, a 3D corona, and a case without a  
 407 hot oxygen corona. Left: case with the 1D globally averaged hot oxygen corona (Case 2). Middle: case with  
 408 the 3D AMPS hot oxygen corona (Case 3). Right: case without the hot oxygen corona (Case 4). Note the use  
 409 of a logarithmic scale.



410 **Figure 9.** The comparison between 1D and 3D exospheric hot oxygen profiles at SZA=0 and SZA=60.

### 411 3.2.2 Effects of 3D Hot Oxygen Corona on Ion Escape: $O^+$ vs. ( $O_2^+$ and $CO_2^+$ )

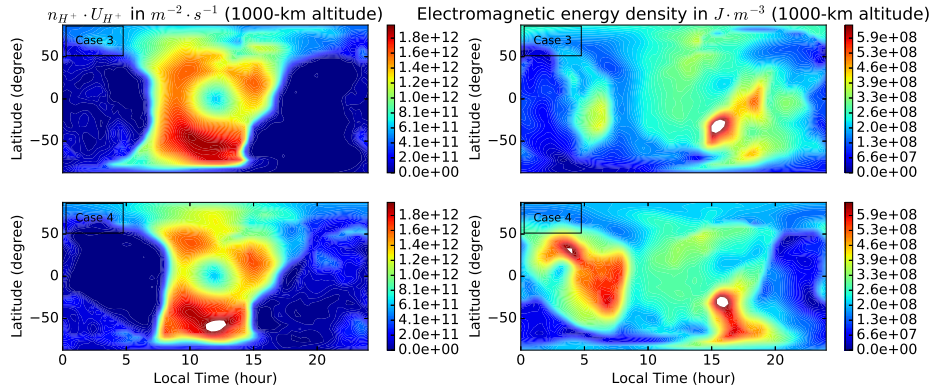
412 In this section, we will focus on Cases 3-4 and aim to understand the effect of a 3D  
 413 hot oxygen on  $O^+$  ion escape versus ionospheric molecular ion ( $O_2^+$  and  $CO_2^+$ ) losses. We  
 414 summarize the calculated ion escape rates for Cases 3-4 in Table 4.

415 Compared with Case 3 that includes hot oxygen, Case 4 (without hot oxygen) has  
 416 higher  $O_2^+$  and  $CO_2^+$  escape rates but maintains a similar value of  $O^+$  escape rate. The  
 417 variation in the molecular to atomic escaping ion ratio (i.e., the last column of Table 4)  
 418 indicates that the hot oxygen component has a shielding effect that can protect the Martian  
 419 ionosphere from the solar wind erosion, especially for  $O_2^+$  and  $CO_2^+$  that have a relatively  
 420 high mass and thus are located at relatively low altitudes. It also reveals that the thermo-

421 spheric oxygen is the dominant neutral source in determining the Martian  $O^+$  ion escape  
422 for APHMOD under the nominal solar wind conditions.

423 Before proceeding further, recall that *Dong et al. [2015a]* calculated the ion escape  
424 rates under different solar cycle and seasonal conditions. They found that  $O_2^+$  is the dom-  
425 inant escaping ion at solar minimum whilst  $O^+$  is the dominant escaping species at so-  
426 lar maximum. *Curry et al. [2013a]* also showed the importance of  $O^+$  ion escape using  
427 a test-particle model at solar maximum. Therefore, we conduct a case study by choosing  
428 Case 10 (autumnal equinox solar maximum - AEQU MAX) in *Dong et al. [2015a]* with  
429 and without 3D hot oxygen corona; the  $O^+$  ion escape rates are  $4.57 \times 10^{24} \text{ s}^{-1}$  and  $3.70$   
430  $\times 10^{24} \text{ s}^{-1}$ , respectively. Compared with APHMOD, the hot oxygen becomes more impor-  
431 tant for  $O^+$  ion escape at AEQU MAX. The thermospheric oxygen atom, however, is still  
432 the primary neutral source for  $O^+$  ion escape for AEQU MAX under the nominal solar  
433 wind conditions.

434 The keys to understand the shielding effect of the hot oxygen corona are the ion  
435 pickup and mass loading processes. Given the momentum and energy conservation, the  
436 solar wind momentum and energy fluxes start to gradually decrease when approaching  
437 Mars due to the mass loading of high-altitude  $O^+$  (ionized from hot oxygen corona). In  
438 the absence of a hot oxygen corona, the solar wind can directly interact with the Martian  
439 ionosphere and thermosphere.



440 **Figure 10.** Comparisons of the solar wind proton number flux,  $n_{H^+}U_{H^+}$  between Case 3 and Case 4  
441 (left). Comparisons of the electromagnetic energy density,  $\mathcal{E}$  between Case 3 and Case 4 (right). Both are  
442 depicted at 1000-km altitude above the Martian surface. The white color highlights the regions beyond the  
443 high saturation of the colorbar.

444 Figure 10 demonstrates the solar wind proton number flux (left) and the electromag-  
445 netic energy density (right) at 1000 km above the Martian surface for Cases 3 and 4. The  
446 electromagnetic energy density is defined as

$$\mathcal{E} = \frac{\epsilon_0 E^2}{2} + \frac{B^2}{2\mu_0} \quad (1)$$

447 where  $\epsilon_0$  and  $\mu_0$  are the permittivity and permeability of free space, respectively.  $E$  de-  
448 notes the electric field (see Eq.(2) in *Dong et al. [2014a]*) and  $B$  represents the magnetic  
449 field. In Figure 10 (left panel), the proton number flux in Case 4 is saturated at 1000-  
450 km altitude (in white) while no saturation is observed in Case 3 using the same colorbar  
451 range. Compared with Case 4, less electromagnetic energy density (right panel of Figure

452 10) is available at same altitude in Case 3, indicating the ionosphere is more disturbed by  
453 the solar wind without a hot oxygen corona.

#### 454 **4 Conclusions**

455 Recently, *Dong et al.* [2017b, 2018] studied the atmospheric ion escape of exoplanets  
456 (such as Proxima b and the TRAPPIST-1 system by assuming Venus-like atmospheres)  
457 orbiting M-dwarfs in the close-in habitable zone. Due to the strong EUV flux and ex-  
458 treme stellar wind parameters, they found that the  $O^+$  ion is always the dominant escap-  
459 ing ion species (due to its relatively small mass and thus large scale height) compared to  
460  $O_2^+$  and  $CO_2^+$ . In certain circumstances, the ionospheric molecular ion ( $O_2^+$  and  $CO_2^+$ ) es-  
461 cape rates of Venus-like exoplanets orbiting M-dwarfs are similar to (and even smaller  
462 than) the cases in our solar system despite the much more intensive stellar radiation and  
463 stellar wind, as a result of the short star-planet distance, e.g. 0.05 AU for Proxima b. The  
464 underlying reason is that the mass loading of relatively light  $O^+$  ion slows down the stel-  
465 lar wind. At ancient times, the EUV flux and solar wind parameters were much stronger  
466 than that of the current epoch (partly resembling those of the M-dwarf exoplanets dis-  
467 cussed earlier), and Mars also has a much more extensive and intensive hot oxygen corona  
468 [Valeille *et al.*, 2010], indicating that hot oxygen exosphere may provide an important  
469 source for  $O^+$  ion escaping billions of years ago. Therefore, the hot oxygen corona may  
470 play a crucial role in the long-term evolution of the Martian atmosphere and its composi-  
471 tion over its history [Dong *et al.*, 2014b]. Based on this study, we speculate that the early  
472 loss rate of the ionospheric molecular ions ( $O_2^+$  and  $CO_2^+$ ) may be even lower than the cur-  
473 rent value due to the strong shielding (i.e., mass loading) effect of high-altitude oxygen  
474 ions.

475 In summary, we studied the solar wind interaction with the Martian upper atmo-  
476 sphere using a one-way coupled framework of three comprehensive 3D models, i.e., the  
477 M-GITM thermosphere output and the Mars AMPS hot atomic oxygen corona are used  
478 as the inputs for the MF-MHD model. The effects of 1D and 3D *cold* thermosphere and  
479 *hot* oxygen corona on the ionospheric structure and ion escape rates are studied in detail  
480 by comparing four selected cases. While the total ion escape rates by adopting 1D and 3D  
481 neutral atmospheres are similar, the detailed ionospheric density distributions are distin-  
482 guishable. Compared with the 1D thermosphere, the MF-MHD calculations based on 3D  
483 thermosphere are in better agreement with MAVEN observations. We also found that the  
484 hot oxygen corona plays an important role in protecting the Martian ionosphere and ther-  
485 mosphere from the solar wind erosion, i.e., reducing the molecular ionospheric ion ( $O_2^+$   
486 and  $CO_2^+$ ) escape rate. The shielding effect can be explained by the mass loading of the  
487 high-altitude hot oxygen ions. Moreover, the simulation results reveal that the *cold* oxygen  
488 is the primary neutral source for  $O^+$  ion escape during this unusually quiet solar cycle.

#### 489 **Acknowledgments**

490 The authors thank M. Lingam for the helpful discussions and comments. This research  
491 was supported by NASA grant NNH10CC04C through MAVEN Project, managed by Lab-  
492 oratory for Atmospheric and Space Physics at the University of Colorado Boulder. It was  
493 also supported by NASA grants 80NSSC18K0288, NNX14AH19G and NNX16AQ04G.  
494 Resources supporting this work were provided by the NASA High-End Computing (HEC)  
495 Program through the NASA Advanced Supercomputing (NAS) Division at Ames Research  
496 Center. We also would like to acknowledge high-performance computing support from  
497 Yellowstone (ark:/85065/d7wd3xhc) and Cheyenne (doi:10.5065/D6RX99HX) provided by  
498 NCAR's Computational and Information Systems Laboratory, sponsored by the National  
499 Science Foundation. The Space Weather Modeling Framework that contains the BATS-R-  
500 US code used in this study is publicly available from <http://csem.engin.umich.edu/tools/swmf>.  
501 The MAVEN data is publicly available through the Planetary Plasma Interactions Node of

502 the Planetary Data System <https://pds-ppi.igpp.ucla.edu/mission/MAVEN>. The  
503 model results are publicly available at <https://umich.box.com/s/tas6l27xzupb4dvkp2whz7k6wklwves3>.

## 504 References

- 505 Acuña, M. H. et al. (1999), Global Distribution of Crustal Magnetization Discovered  
506 by the Mars Global Surveyor MAG/ER Experiment, *Science*, 284, 790–793, doi:  
507 10.1126/science.279.5357.1676.
- 508 Arkani-Hamed, J. (2001), A 50-degree spherical harmonic model of the magnetic field of  
509 Mars, *Journal of Geophysical Research*, 106, 23,197–23,208.
- 510 Bird, G. A., (1994), *Molecular Gas Dynamics and the Direct Simulation of Gas Flows*,  
511 2nd ed., Clarendon Press, Oxford.
- 512 Bougher, S. W., P.-L. Blelly, M. R. Combi, J. L. Fox, I. Mueller-Wodarg, A. Ridley, and  
513 R. G. Roble (2008), Neutral Upper Atmosphere and Ionosphere Modeling, *Space Sci.*  
514 *Reviews*, 139, 107–141, doi:10.1007/s11214-008-9401-9.
- 515 Bougher, S. W., D. J. Pawlowski, J. M. Bell, S. Nelli, T. McDunn, J. R. Murphy, M.  
516 Chizek, and A. Ridley (2015a), Mars global ionosphere-thermosphere model (MGITM):  
517 Solar cycle, seasonal, and diurnal variations of the Mars upper atmosphere, *Journal of*  
518 *Geophysical Research*, 120 311–342, doi:10.1002/2014JE004715.
- 519 Bougher, S., et al. (2015b), Early MAVEN Deep Dip campaign reveals thermosphere and  
520 ionosphere variability, *Science*, 350, 0459, doi:10.1126/science.aad0459.
- 521 Bougher, S. W., T. E. Cravens, J. Grebowsky, and J. Luhmann (2015c), The Aeronomy of  
522 Mars: Characterization by MAVEN of the Upper Atmosphere Reservoir that Regulates  
523 Volatile Escape, *Space Science Reviews*, 195, 423–456, doi:10.1007/s11214-014-0053-7.
- 524 Bougher, S. W., K. Roeten, K. Olsen, P. R. Mahaffy, M. Benna, M. Elrod, S. Jain, N. M.  
525 Schneider, J. Deighan, E. Thiemann, F. G. Eparvier, A. Stiepen, and B. Jakosky (2017),  
526 The structure and variability of Mars dayside thermosphere from MAVEN NGIMS and  
527 IUVS measurements: Seasonal and solar activity trends in scale heights and tempera-  
528 tures, *Journal of Geophysical Research*, 122, 1296–1313, doi:10.1002/2016JA023454.
- 529 Brain, D. A., J. P. McFadden, J. S. Halekas, J. E. P. Connerney, S. W. Bougher, S. Curry,  
530 C. F. Dong, Y. Dong, F. Eparvier, X. Fang, K. Fortier, T. Hara, Y. Harada, B. M.  
531 Jakosky, R. J. Lillis, R. Livi, J. G. Luhmann, Y. Ma, R. Modolo, and K. Seki (2015),  
532 The spatial distribution of planetary ion fluxes near Mars observed by MAVEN, *Geo-*  
533 *phys. Res. Lett.*, 42, 9142–9148, doi:10.1002/2015GL065293.
- 534 Brecht, S. H., S. A. Ledvina and S. W. Bougher (2016), Ionospheric loss from Mars as  
535 predicted by hybrid particle simulations, *J. Geophys. Res. Space Physics*, 121, 10,190–  
536 10,208.
- 537 Cravens, T. E., J. U. Kozyra, A. F. Nagy, T. I. Gombosi, and M. Kurtz (1987), Electron  
538 impact ionization in the vicinity of comets, *Journal of Geophysical Research*, 92, 7341–  
539 7353.
- 540 Cravens, T. E., Hamil, O., Houston, S., Bougher, S., Ma, Y., Brain, D. and Ledvina, S.  
541 (2017), Estimates of ionospheric transport and ion loss at Mars, *Journal of Geophysical*  
542 *Research: Space Physics*, 122, 10,626–10,637.
- 543 Curry, S. M., M. W. Liemohn, X.-H. Fang, Y.-J. Ma, J. Espley (2013a), The influence of  
544 production mechanisms on pick-up ion loss at Mars, *Journal of Geophysical Research*,  
545 118, 554–569, doi:10.1029/2012JA017665.
- 546 Curry, S. M., M. Liemohn, X. Fang, D. Brain, and Y. Ma (2013b), Simulated kinetic ef-  
547 fects of the corona and solar cycle on high altitude ion transport at Mars, *Journal of*  
548 *Geophysical Research*, 118, 3700–3711, doi:10.1002/jgra.50358.
- 549 Curry, S. M., M. W. Liemohn, X.-H. Fang, Y.-J. Ma, J. Slavin, J. Espley, S. Bougher,  
550 and C. F. Dong (2014), Test particle comparison of heavy atomic and molecular  
551 ion distributions at Mars, *Journal of Geophysical Research*, 119, 2328–2344, doi:  
552 10.1002/2013JA019221.

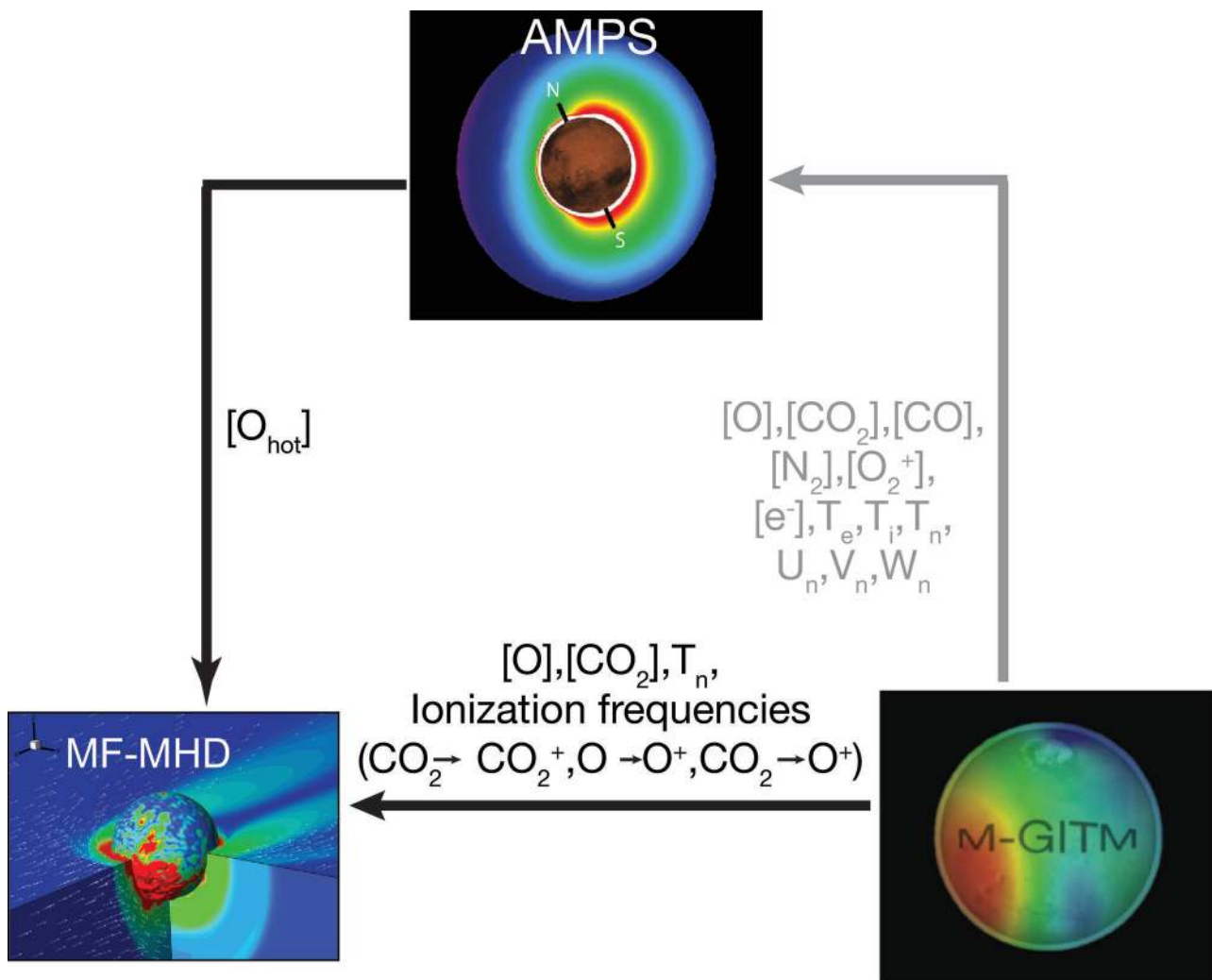
- 553 Curry, S. M., J. G. Luhmann, Y. Ma, M. W. Liemohn, C. Dong, and T. Hara  
554 (2015a), Comparative pick-up ion distributions at Mars and Venus: Consequences  
555 for atmospheric deposition and escape, *Planet. Space Sci.*, *115*, 35–47, doi:  
556 10.1016/j.pss.2015.03.026.
- 557 Curry, S. M., J. G. Luhmann, Y. J. Ma, C. F. Dong, D. Brain, F. Leblanc, R. Modolo,  
558 Y. Dong, J. McFadden, J. Halekas, J.E.P. Connerney, J. Espley, T. Hara, Y. Harada, C.  
559 Lee, X. Fang, and B. Jakosky (2015b), Response of Mars O<sup>+</sup> Pick-up Ions to the March  
560 8th, 2015 ICME: Inferences from MAVEN Data-Based Models, *Geophys. Res. Lett.*, *42*,  
561 9095–9102, doi:10.1002/2015GL065304.
- 562 Deng, Y., A. D. Richmond, A. J. Ridley, and H.-L. Liu (2008), Assessment of the non-  
563 hydrostatic effect on the upper atmosphere using a general circulation model (GCM),  
564 *Geophysical Research Letters*, *35*, L01104, doi:10.1029/2007GL032182
- 565 DiBraccio, G. A., J. G. Luhmann, S. M. Curry, J. R. Espley, S. Xu, D. L. Mitchell, Y. Ma,  
566 C. Dong, J. R. Gruesbeck, J. E. P. Connerney, Y. Harada, S. Ruhunusiri, J. S. Halekas,  
567 Y. Soobiah, T. Hara, D. A. Brain, B. M. Jakosky (2018), The Twisted Configuration  
568 of the Martian Magnetotail: MAVEN Observations, *Geophysical Research Letters*, doi:  
569 10.1029/2018GL077251.
- 570 Dong, C., S. W. Bougher, Y. Ma, G. Toth, A. F. Nagy, and D. Najib (2014a), Solar wind  
571 interaction with Mars upper atmosphere: Results from the one-way coupling between  
572 the multifluid MHD model and the MTGCM model, *Geophysical Research Letters*, *41*,  
573 2708–2715, doi:10.1002/2014GL059515.
- 574 Dong, C., S. W. Bougher, Y. Ma, G. Toth, Y. Lee, A. F. Nagy, V. Tennishev, D. Pawlowski  
575 and M. Combi (2014b), Solar Wind Interaction with the Martian Upper Atmosphere at  
576 Early Mars/Extreme Solar Conditions, *AGU Fall Meeting Abstracts*, abstract P53C-4032.
- 577 Dong, C., S. W. Bougher, Y. Ma, G. Toth, Y. Lee, A. F. Nagy, V. Tennishev, D. J.  
578 Pawlowski, M. R. Combi, and D. Najib (2015a), Solar wind interaction with the Mar-  
579 tian upper atmosphere: Crustal field orientation, solar cycle and seasonal variations, *J.*  
580 *Geophys. Res. Space Physics*, *120*, 7857–7872, doi:10.1002/2015JA020990.
- 581 Dong, C., Y. Ma, S. W. Bougher, G. Toth, A. F. Nagy, J. S. Halekas, Y. Dong, S. M.  
582 Curry, J. G. Luhmann, D. Brain, J. E. P. Connerney, J. Espley, P. Mahaffy, M. Benna,  
583 J. P. McFadden, D. L. Mitchell, G. A. DiBraccio, R. J. Lillis, B. M. Jakosky, and J. M.  
584 Grebowsky (2015b), Multifluid MHD study of the solar wind interaction with Mars' up-  
585 per atmosphere during the 2015 March 8th ICME event, *Geophysical Research Letters*,  
586 *42*, 9103–9112, doi:10.1002/2015GL065944.
- 587 Dong, C., Z. Huang, M. Lingam, G. Toth, T. Gombosi, and A. Bhattacharjee (2017a), The  
588 dehydration of water worlds via atmospheric losses, *ApJ Letters*, *847*, L4.
- 589 Dong, C., M. Lingam, Y. J. Ma, and O. Cohen (2017b), Is Proxima Centauri B habitable?  
590 A study of atmospheric loss, *ApJ Letters*, *837*, L26.
- 591 Dong, C., M. Jin, M. Lingam, V. S. Airapetian, Y. J. Ma, B. van der Holst (2018), Atmo-  
592 spheric escape from the TRAPPIST-1 planets and implications for habitability, *Proceed-*  
593 *ings of the National Academy of Sciences*, *115*, 260–265, doi:10.1073/pnas.1708010115.
- 594 Dong, Y., X. Fang, D. A. Brain, J. P. McFadden, J. S. Halekas, J. E. Connerney, S. M.  
595 Curry, Y. Harada, J. G. Luhmann, B. M. Jakosky (2015c), Strong plume fluxes at Mars  
596 observed by MAVEN: An important planetary ion escape channel, *Geophysical Re-*  
597 *search Letters*, *42*, 8942–8950, doi:10.1002/2015GL065346.
- 598 Egan, H., Y. Ma, C. Dong, R. Modolo, R. Jarvinen, S. Bougher, J. Halekas, D. Brain, J.  
599 McFadden, J. Connerney, D. Mitchell, B. Jakosky (2018), Comparison of Global Mar-  
600 tian Plasma Models in the Context of MAVEN Observations, *J. Geophys. Res. Space*  
601 *Physics*, doi:10.1029/2017JA025068.
- 602 Fang, X., M. W. Liemohn, A. F. Nagy, Y. Ma, D. L. De Zeeuw, J. U. Kozyra, and T. H.  
603 Zurbuchen (2008), Pickup oxygen ion velocity space and spatial distribution around  
604 Mars, *J. Geophys. Res.*, *113*, A02210, doi:10.1029/2007JA012736.
- 605 Fang, X., M. W. Liemohn, A. F. Nagy, J. G. Luhmann, and Y. J. Ma (2010a), On the ef-  
606 fect of the martian crustal magnetic field on atmospheric erosion, *Icarus*, *206*, 130–138,

- doi:10.1016/j.icarus.2009.01.012.
- 607 Fang, X., M. W. Liemohn, A. F. Nagy, J. G. Luhmann, and Y. Ma (2010b), Escape prob-  
608 ability of Martian atmospheric ions: Controlling effects of the electromagnetic fields, *J.*  
609 *Geophys. Res.*, *115*, A04308, doi:10.1029/2009JA014929.
- 610 Fang, X., Y. J. Ma, K. Masunaga, Y. X. Dong, D. Brain, J. Halekas, R. Lillis, B. Jakosky,  
611 J. Connerney, J. Grebowsky, and C. F. Dong (2017), A quantitative study of the Mars  
612 crustal magnetic field control of plasma boundary locations and atmospheric loss: MHD  
613 prediction and comparison with MAVEN observations, *J. Geophys. Res. Space Physics*,  
614 *122*, 4117–4137, doi:10.1002/2016JA023509.
- 615 Glocer, A., G. Tóth, Y. J. Ma, T. I. Gombosi, J. C. Zhang, and L. M. Kistler (2009), Mul-  
616 tifluid Block-Adaptive-Tree Solar Wind Roe-Type Upwind Scheme: Magnetospheric  
617 composition and dynamics during geomagnetic storms—Initial results, *J. Geophys. Res.*,  
618 *114*, A12203, doi:10.1029/2009JA014418.
- 619 Halekas, J. S., D. A. Brain, S. Ruhunusiri, J. P. McFadden, D. L. Mitchell, C. Mazelle,  
620 J. E. P. Connerney, Y. Harada, T. Hara, J. R. Espley, G. A. DiBraccio, B. M. Jakosky  
621 (2016), Plasma clouds and snowplows: Bulk plasma escape from Mars observed by  
622 MAVEN, *Geophys. Res. Lett.*, *43*, 1426–1434, doi:10.1002/2016GL067752.
- 623 Hanson, W. B., S. Sanatini, and D. R. Zuccaro (1977), The Martian ionosphere as ob-  
624 served by the Viking retarding potential analyzer, *J. Geophys. Res.*, *82*, 4351–4363.
- 625 Harnett, E. M., and R. M. Winglee (2006), Three-dimensional multifluid simulations of  
626 ionospheric loss at Mars from nominal solar wind conditions to magnetic cloud events,  
627 *J. Geophys. Res.*, *111*, A09213, doi:10.1029/2006JA011724.
- 628 Hassler, D. M., C. Zeitlin, R. F. Wimmer-Schweingruber, et al. (2014), Mars’ Surface Ra-  
629 diation Environment Measured with the Mars Science Laboratory’s Curiosity Rover,  
630 *Science*, *343*, 1244797.
- 631 Huang, Z. G., G. Toth, T. I. Gombosi, X. Z. Jia, M. Rubin, N. Fougere, V. Teni-  
632 shev, M. R. Combi, A. Bieler, K. C. Hansen, Y. S. Shou, K. Altwegg (2016),  
633 Four-fluid MHD simulations of the plasma and neutral gas environment of comet  
634 67P/Churyumov-Gerasimenko near perihelion, *J. Geophys. Res.*, *121*, 4247–4268, doi:  
635 10.1002/2015JA022333.
- 636 Ip, W. H. (1988), On a hot oxygen corona of Mars, *Icarus*, *76*, 135.
- 637 Jakosky, B. M. et al. (2015a), The Mars Atmosphere and Volatile Evolution (MAVEN)  
638 Mission, *Space Science Reviews*, *195*, 3–48, doi:10.1007/s11214-015-0139-x.
- 639 Jakosky, B. M., et al. (2015b), MAVEN observations of the response of Mars to an inter-  
640 planetary coronal mass ejection, *Science*, *350*, 0210, doi:10.1126/science.aad0210.
- 641 Johnson, R. E., J. G. Luhmann (1998), Sputter contribution to the atmospheric corona on  
642 Mars, *J. Geophys. Res.*, *103*, 3649–3653.
- 643 Kharchenko, V., A. Dalgarno, B. Zygelman, and J. H. Yee (2000), Energy transfer in col-  
644 lisions of oxygen atoms in the terrestrial atmosphere, *J. Geophys. Res.*, *103*, 24,899–  
645 24,906.
- 646 Kim, J., A. F. Nagy, J. L. Fox, and T. E. Cravens (1998), Solar cycle variability of hot  
647 oxygen atoms at Mars, *J. Geophys. Res.*, *103*, 29,339.
- 648 Leblanc, F., J. Y. Chaufray, R. Modolo, L. Leclercq, S. Curry, J. Luhmann, R. Lillis, T.  
649 Hara, J. McFadden, J. Halekas, N. Schneider, J. Deighan, P. R. Mahaffy, M. Benna, R.  
650 E. Johnson, F. Gonzalez-Galindo, F. Forget, M. A. Lopez-Valverde, F. G. Eparvier, B.  
651 Jakosky (2017), On the Origins of Mars’ Exospheric Nonthermal Oxygen Component as  
652 Observed by MAVEN and Modeled by HELIOSARES, *J. Geophys. Res. Planets*, *122*,  
653 2401–2428, doi:10.1002/2017JE005336.
- 654 Leblanc, F., A. Martinez, J. Y. Chaufray, R. Modolo, T. Hara, J. Luhmann, R. Lillis, S.  
655 Curry, J. McFadden, J. Halekas, B. Jakosky (2018), On Mars’ Atmospheric Sputtering  
656 after MAVEN first Martian year of Measurements, *Geophysical Research Letters*, doi:  
657 10.1002/2018GL077199.
- 658 Lee, Y., M. R. Combi, V. Tenishev, S. W. Bougher, and R. J. Lillis (2015a), Hot oxygen  
659 corona at Mars and the photochemical escape of oxygen: Improved description of the  
660

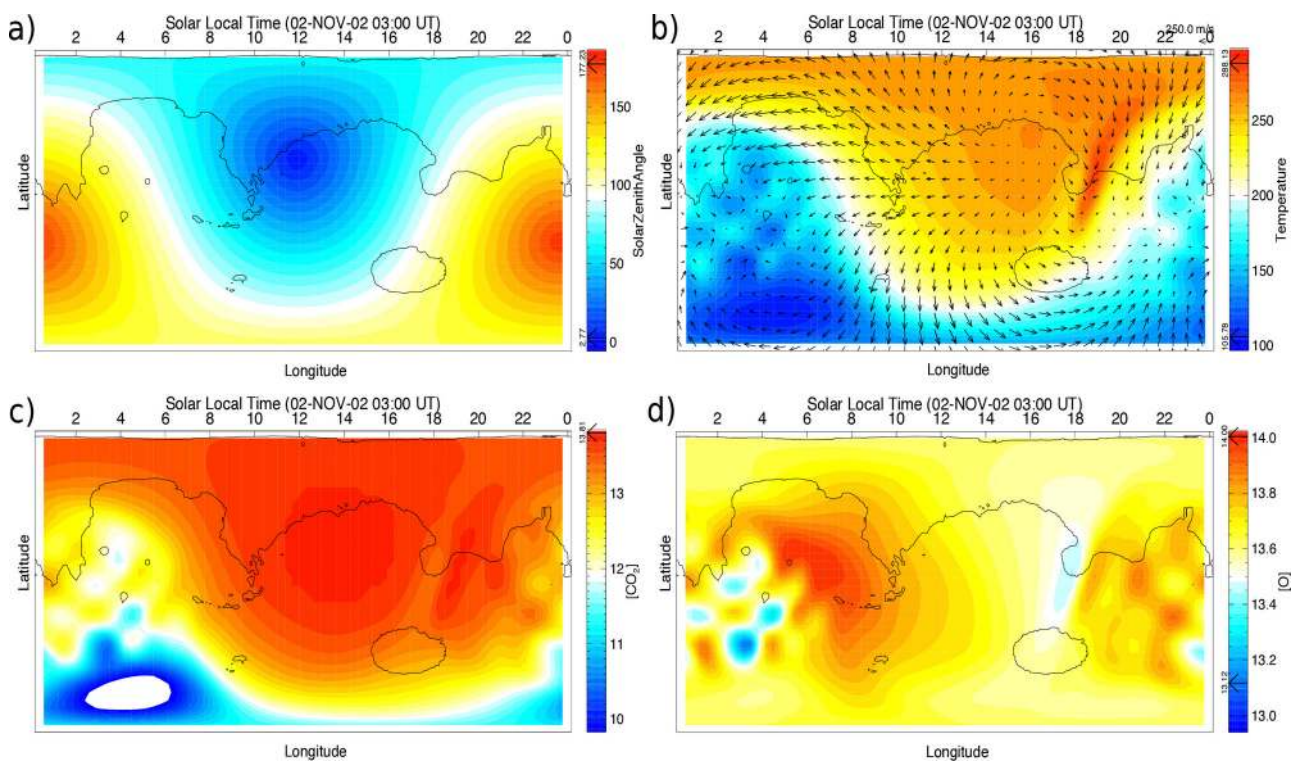
- 661 thermosphere, ionosphere, and exosphere, *Journal of Geophysical Research (Planets)*,  
662 120, 1880–1892, doi:10.1002/2015JE004890.
- 663 Lee, Y., M. R. Combi, V. Tennishev, S. W. Bougher, J. Deighan, N. M. Schneider, W. E.  
664 McClintock, B. M. Jakosky (2015b), A comparison of 3-D model predictions of Mars'  
665 oxygen corona with early MAVEN IUVS observations, *Geophysical Research Letters*,  
666 42, 9015–9022, doi:10.1002/2015GL065291.
- 667 Liemohn, M. W., B. C. Johnson, M. Franz, and S. Barabash (2014), Mars Express  
668 observations of high altitude planetary ion beams and their relation to the “ener-  
669 getic plume” loss channel, *J. Geophys. Res. Space Physics*, 119, 9702–9713, doi:  
670 10.1002/2014JA019994.
- 671 Liemohn, M. W., S. Xu, C. Dong, S. W. Bougher, B. C. Johnson, R. Ilie, and D. L.  
672 De Zeeuw (2017), Ionospheric control of the dawn-dusk asymmetry of the Mars  
673 magnetotail current sheet, *J. Geophys. Res. Space Physics*, 122, 6397–6414, doi:  
674 10.1002/2016JA023707.
- 675 Lillis, R. J., D. A. Brain, S. W. Bougher, F. Leblanc, J. G. Luhmann, B. M. Jakosky,  
676 R. Modolo, J. Fox, J. Deighan, X. Fang, Y. C. Wang, Y. Lee, C. Dong, Y. Ma,  
677 T. Cravens, L. Andersson, S. M. Curry, N. Schneider, M. Combi, I. Stewart, J. Clarke,  
678 J. Grebowsky, D. L. Mitchell, R. Yelle, A. F. Nagy, D. Baker, and R. P. Lin (2015),  
679 Characterizing Atmospheric Escape from Mars Today and Through Time, with  
680 MAVEN, *SSRv*, 195, 357–422, doi:10.1007/s11214-015-0165-8.
- 681 Fox, J. L. (1993), On the escape of oxygen and hydrogen from Mars, *Geophys. Res. Lett.*,  
682 20, 1747–1750.
- 683 Lingam, M., C. F. Dong, X. H. Fang, B. M. Jakosky, A. Loeb (2018), The propitious role  
684 of solar energetic particles in the origin of life, *ApJ*, 853, 10.
- 685 Luhmann, J. G., and J. U. Kozyra (1991), Dayside pickup oxygen ion precipitation at  
686 Venus and Mars: Spatial distributions, energy deposition and consequences, *J. Geophys.*  
687 *Res.*, 96(A4), 5457–5467, doi:10.1029/90JA01753.
- 688 Luhmann, J. G., C.F. Dong, Y.J. Ma, S.M. Curry, D. Mitchell, J. Espley, J. Connerney, J.  
689 Halekas, D.A. Brain, B.M. Jakosky, and C. Mazelle (2015), Implications of MAVEN  
690 Mars Near-Wake Measurements and Models, *Geophys. Res. Lett.*, 42, 9087–9094, doi:  
691 10.1002/2015GL066122.
- 692 Luhmann, J. G., C. F. Dong, Y. J. Ma, S. M. Curry, S. Xu, C. O. Lee, T. Hara, J. Halekas,  
693 Yan Li, J. R. Gruesbeck, J. Espley, D. A. Brain, C. T. Russell (2017), Martian Magnetic  
694 Storms, *J. Geophys. Res. Space Physics*, 122, 6185–6209, doi:10.1002/2016JA023513 .
- 695 Lundin, R., S. Barabash, M. Holmström, H. Nilsson, Y. Futaana, R. Ramstad, M. Ya-  
696 mauchi, E. M. Dubinin, and M. Fraenz, (2013), Solar cycle effects on the ion escape  
697 from Mars, *Geophysical Research Letters*, 40, 6028–6032, doi:10.1002/2013GL058154.
- 698 Ma, Y. J., A. F. Nagy, I. V. Sokolov, and K. C. Hansen (2004), Three-dimensional, multi-  
699 species, high spatial resolution MHD studies of the solar wind interaction with Mars, *J.*  
700 *Geophys. Res. Space Physics*, 109, A07,211, doi:10.1029/2003JA010367.
- 701 Ma, Y. J., X. Fang, C. T. Russell, A. F. Nagy, G. Toth, J. G. Luhmann, D. A. Brain, and  
702 C. Dong (2014), Effects of crustal field rotation on the solar wind plasma interaction  
703 with Mars, *Geophysical Research Letters*, 41, doi:10.1002/2014GL060785.
- 704 Ma, Y. J., C. T. Russell, X. Fang, C. F. Dong, A. F. Nagy, G. Toth, J. S. Halekas, J. E. P.  
705 Connerney, J. R. Espley, P. R. Mahaffy, M. Benna, J. McFadden, D. Mitchell, L. Ander-  
706 sson, and B. M. Jakosky (2017), Variations of the Martian plasma environment during  
707 the ICME passage on 8 March 2015 – A time-dependent MHD study , *J. Geophys. Res.*  
708 *Space Physics*, 41, 1714–1730, doi:10.1002/2016JA023402.
- 709 Modolo, R., et al. (2016), Mars-solar wind interaction: LatHyS, an improved parallel 3-  
710 D multispecies hybrid model, *J. Geophys. Res. Space Physics*, 121, 6378–6399, doi:  
711 10.1002/2015JA022324.
- 712 Nagy, A. F., and T. E. Cravens (1988), Hot oxygen atoms in the upper atmosphere of  
713 Venus and Mars, *Geophys. Res. Lett.*, 15, 433–435, doi:10.1029/GL015i005p00433.



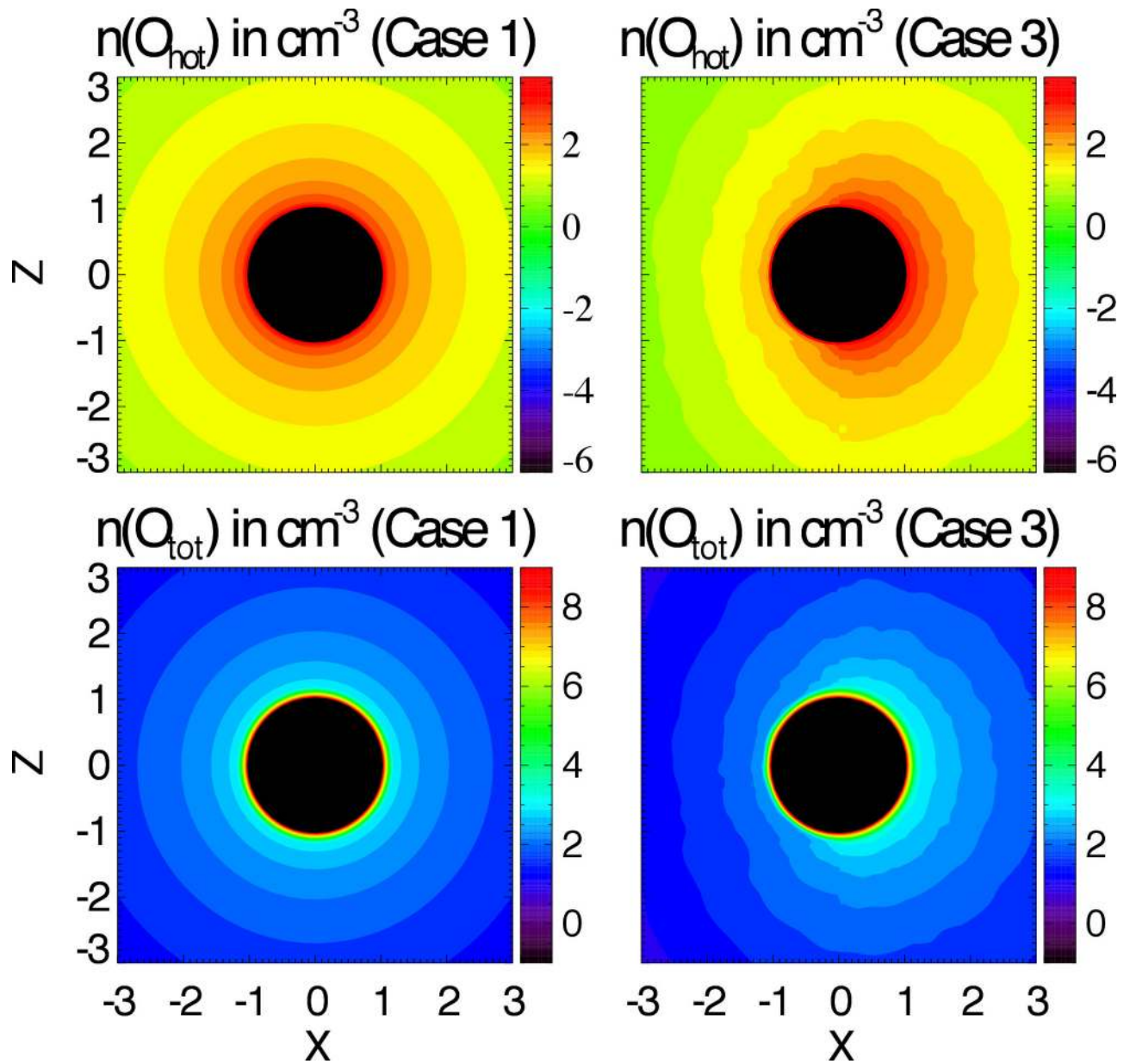
- 714 Najib, D., A. F. Nagy, G. Tóth, and Y. J. Ma (2011), Three-dimensional, multifluid, high  
715 spatial resolution MHD model studies of the solar wind interaction with Mars, *Journal*  
716 *of Geophysical Research*, *116*, A05,204, doi:10.1029/2010JA016272.
- 717 Powell, K. G., P. L. Roe, T. J. Linde, T. I. Gombosi, and D. L. De Zeeuw (1999), A  
718 Solution-Adaptive Upwind Scheme for Ideal Magnetohydrodynamics, *J. Computational*  
719 *Phys.*, *154*, 284–309.
- 720 Ramstad, R., S. Barabash, Y. Futaana, H. Nilsson, X.-D. Wang, M. Holmström (2015),  
721 The Martian atmospheric ion escape rate dependence on solar wind and solar EUV con-  
722 ditions I: Seven years of Mars Express observations, *Journal of Geophysical Research*,  
723 doi:10.1002/2015JE004816.
- 724 Ridley, A., Y. Deng, and G. Toth (2006), The global ionosphere-thermosphere model, *J.*  
725 *Atmos. Sol-Terr. Phys.*, *68*, 839.
- 726 Rioussset, J. A., C. S. Paty, R. J. Lillis, M. O. Fillingim, S. L. England, P. G. Withers, and  
727 J. P. M. Hale (2013), Three-dimensional multifluid modeling of atmospheric electro-  
728 dynamics in Mars' dynamo region, *Journal of Geophysical Research*, *118*, 1–13, doi:  
729 10.1002/jgra.50328.
- 730 Rioussset, J. A., C. S. Paty, R. J. Lillis, M. O. Fillingim, S. L. England, P. G. With-  
731 ers, and J. P. M. Hale (2014), Electrodynamics of the Martian dynamo region  
732 near magnetic cusps and loops, *Geophysical Research Letters*, *41*, 1119–1125, doi:  
733 10.1002/2013GL059130.
- 734 Rubin, M., , et al. (2014), Plasma environment of a weak comet - Predictions for Comet  
735 67P/Churyumov-Gerasimenko from multifluid-MHD and Hybrid models, *Icarus*, *242*,  
736 38–49.
- 737 Schunk, R. W., and A. F. Nagy (2009), *Ionospheres*, 2nd ed., Cambridge Univ. Press, New  
738 York, pp102–109, chapter 8, pp 483.
- 739 Smith F. L., and C. Smith (1972), Numerical evaluation of Chapman's grazing inci-  
740 dence integral ch (X, X), *Journal of Geophysical Research*, *77*, 3592–3597, doi:  
741 10.1029/JA077i019p03592.
- 742 Tenishev, V., and M. Combi (2008), A global kinetic model for cometary comae: The evo-  
743 lution of the coma of the Rosetta target comet Churyumov-Gerasimenko throughout the  
744 mission, *ApJ*, *685*, 659–677.
- 745 Tenishev, V., M. Rubin, O. J. Tucker, M. R. Combi, and M. Sarantos (2013a), Ki-  
746 netic modeling of sodium in the lunar exosphere, *Icarus*, *226*, 1538–1549, doi:  
747 10.1016/j.icarus.2013.08.021.
- 748 Tóth, G. et al. (2012), Adaptive Numerical Algorithms in Space Weather Modeling, *J.*  
749 *Computational Phys.*, *231*, 870–903, doi:10.1016/j.jcp.2011.02.006.
- 750 Valeille, A., V. Tenishev, S. W. Bougher, M. R. Combi, and A. F. Nagy (2009), Three-  
751 dimensional study of Mars upper thermosphere/ionosphere and hot oxygen corona: 1.  
752 General description and results at equinox for solar low conditions, *Journal of Geophys-*  
753 *ical Research*, *114*, E11005, doi:10.1029/2009JE003388
- 754 Valeille, A., S. W. Bougher, V. Tenishev, M. R. Combi, A. F. Nagy (2010), Water loss and  
755 evolution of the upper atmosphere and exosphere over martian history, *Icarus*, *206*, 28–  
756 39, doi:10.1016/j.icarus.2009.04.036.
- 757 Wallis, M. K. (1978), Exospheric density and escape fluxes of atomic isotopes on Venus  
758 and Mars, *Planet. Space Sci.*, *26*, 949.
- 759 Withers, P., M. Vogt, M. Mayyasi, P. Mahaffy, M. Benna, M. Elrod, S. Bougher, C.F.  
760 Dong, J.-Y. Chaufray, Y.J. Ma, and B. Jakosky (2015), Comparison of model predictions  
761 for the composition of the ionosphere of Mars to MAVEN NGIMS data, *Geophys. Res.*  
762 *Let.*, *42*, 8966–8976, doi:10.1002/2015GL065205.
- 763 Xu, S., D. Mitchell, M. W. Liemohn, C. F. Dong, S. Bougher, M. Fillingim, R. Lillis, J.  
764 McFadden, C. Mazelle, J. Connerney, and B. Jakosky (2016), Deep nightside photoelec-  
765 tron observations by MAVEN SWEA: implications for Martian northern-hemispheric  
766 magnetic topology and nightside ionosphere source, *Geophys. Res. Let.*, *43*, 8876–8884,  
767 doi:10.1002/2016GL070527.



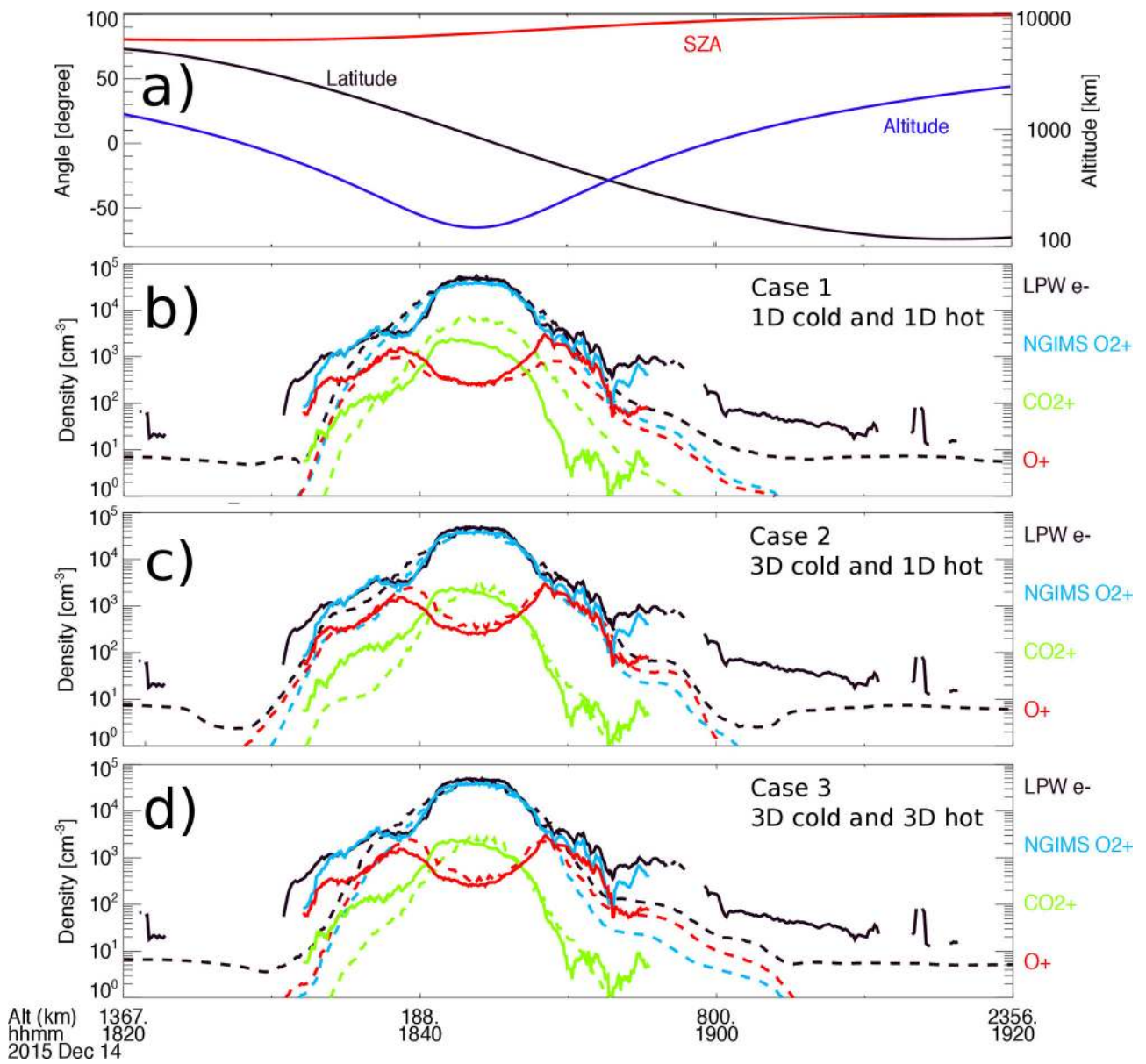
2018ja025543-f01-z-eps

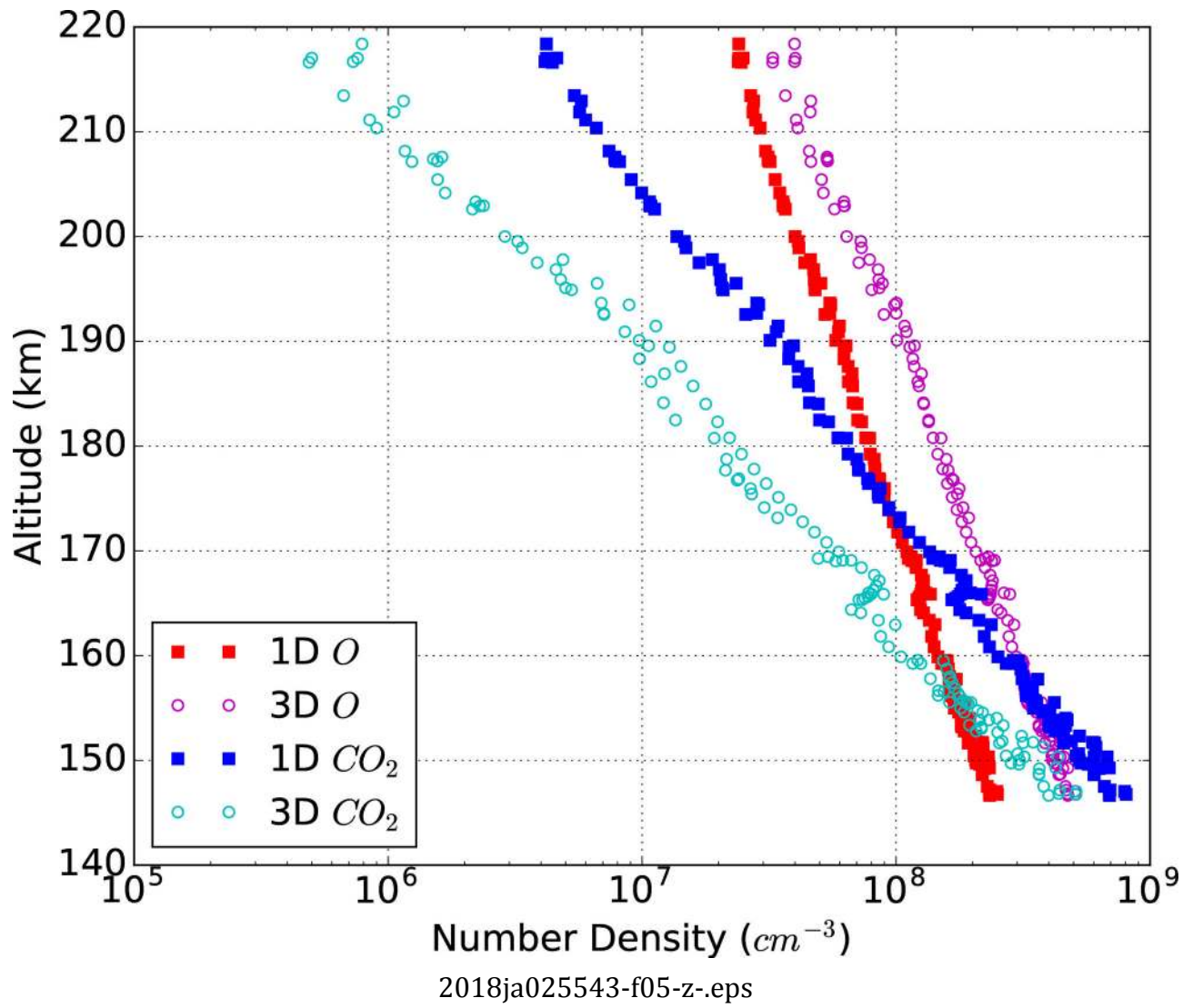


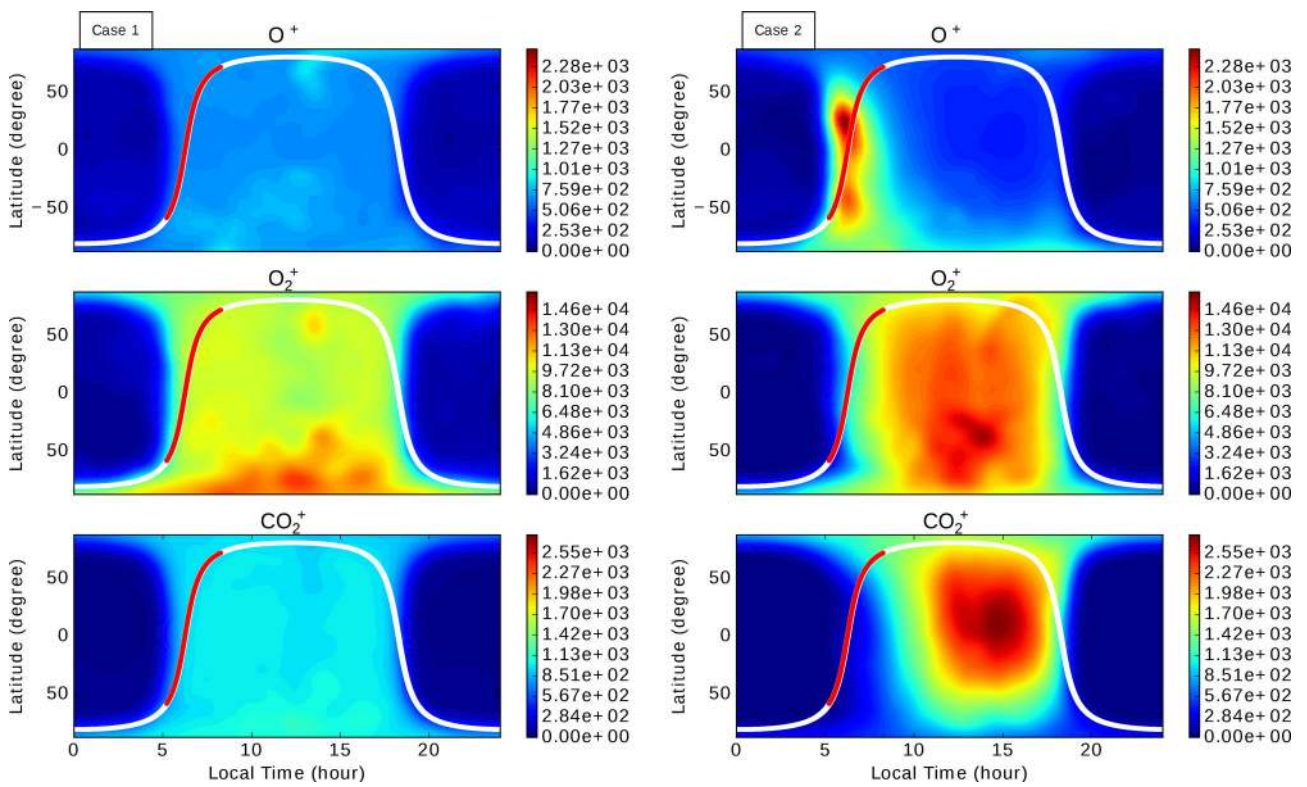
2018ja025543-f02-z-.eps



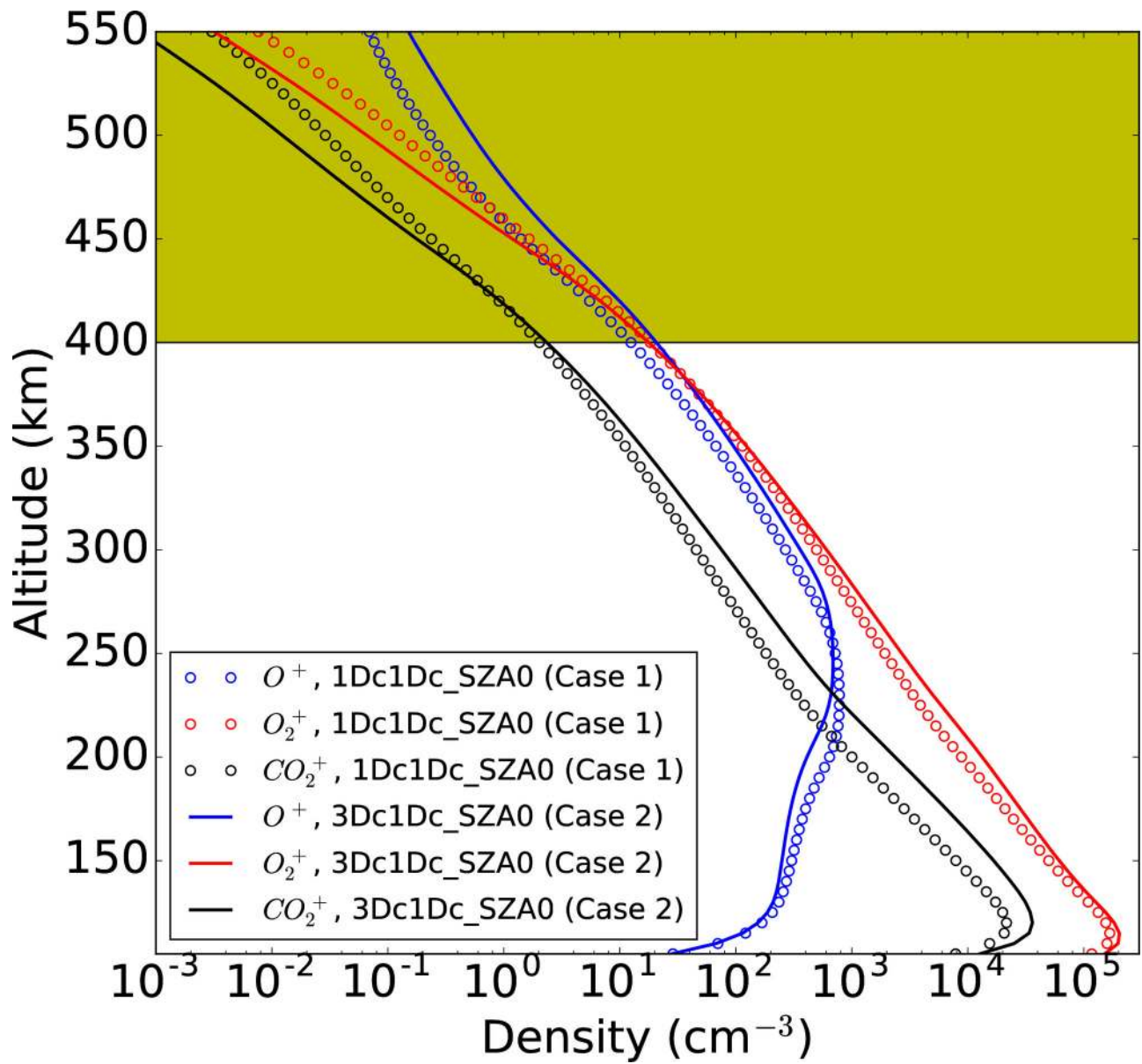
2018ja025543-f03-z-.eps





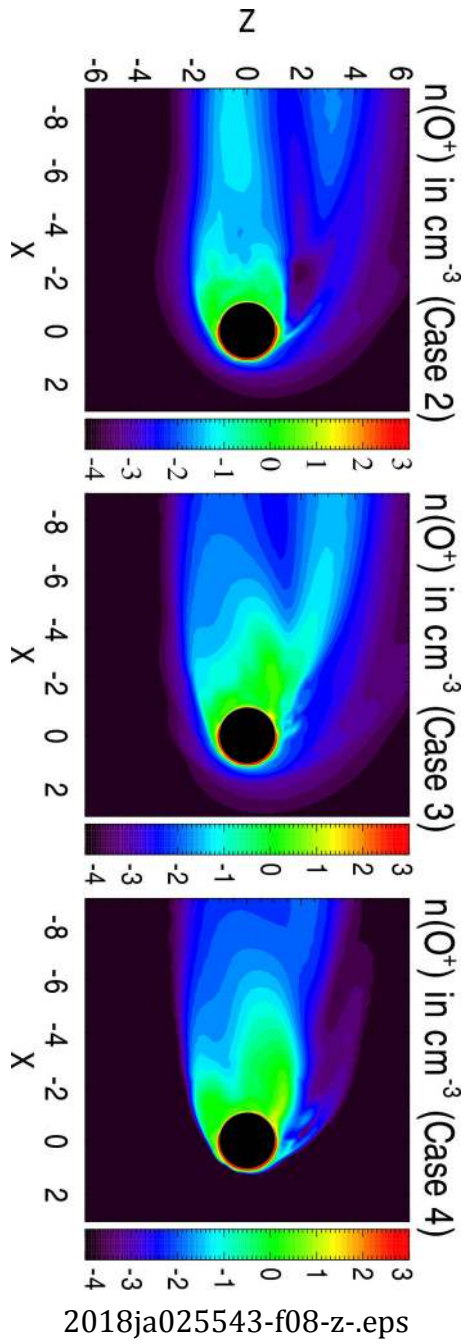


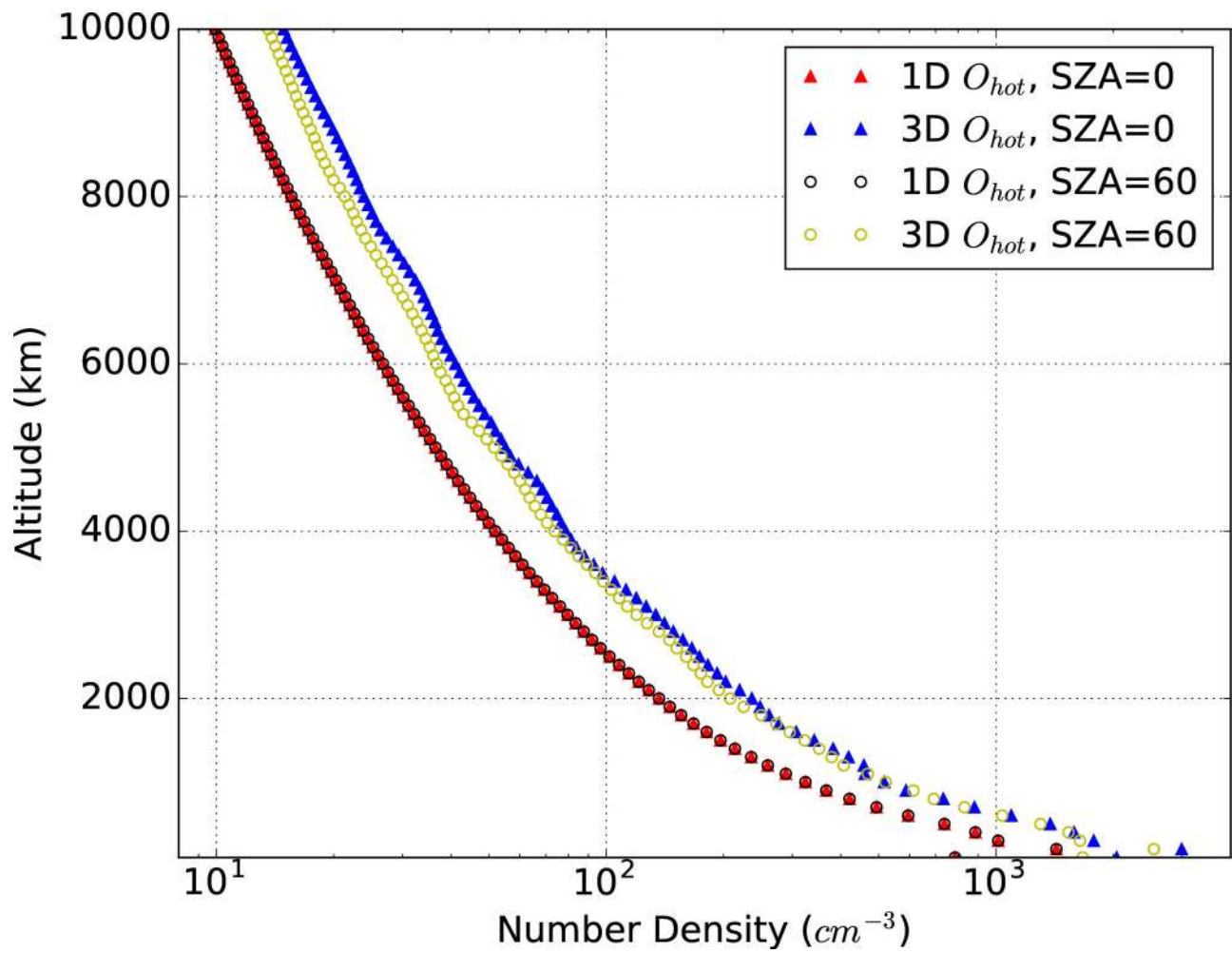
2018ja025543-f06-z-eps

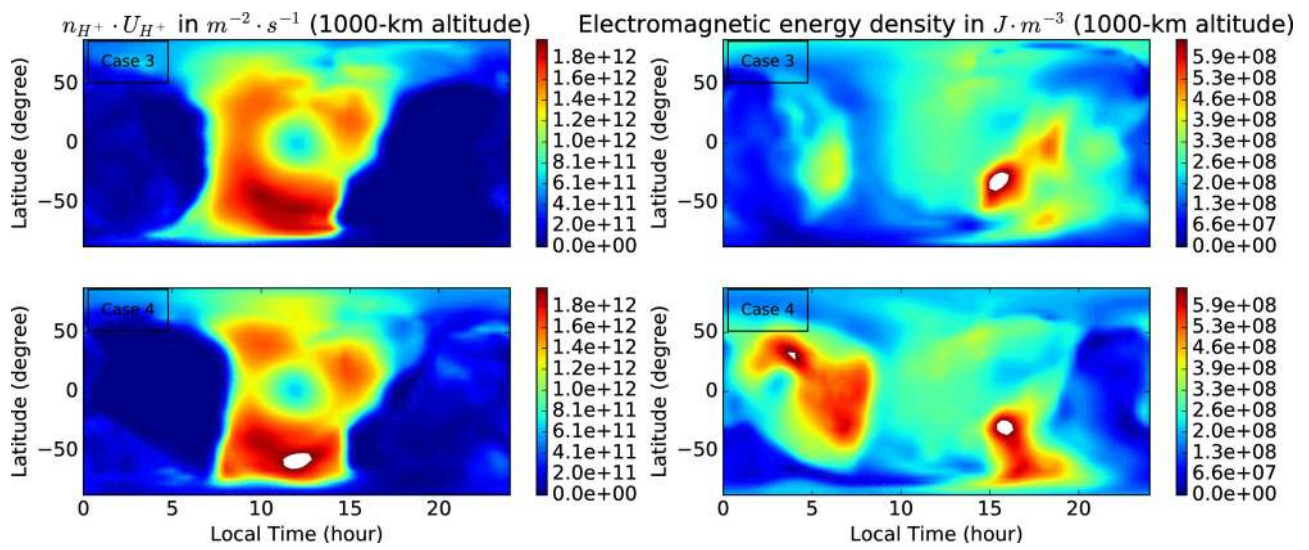


2018ja025543-f07-z-.eps









2018ja025543-f10-z-eps